



# OpenFOAM-avalanche 2312: Depth-integrated Models Beyond Dense Flow Avalanches

Matthias Rauter<sup>1,2</sup> and Julia Kowalski<sup>3</sup>

<sup>1</sup>Unit of Geotechnical Engineering, University of Innsbruck, Innsbruck, Austria

<sup>2</sup>Department of Civil Engineering and Natural Hazards, University of Natural Resources and Life Sciences, Vienna, Austria

<sup>3</sup>Methods for Model-based Development in Computational Engineering, RWTH Aachen University, Aachen, Germany

**Correspondence:** Julia Kowalski (kowalski@mbd.rwth-aachen.de)

**Abstract.** Numerical simulations have become an important tool for the estimation and mitigation of gravitational mass flows, such as avalanches, landslides, pyroclastic flows or turbidity currents. Depth-integration stands as a pivotal concept in rendering numerical models applicable to real-world scenarios, as it provides the required efficiency and a streamlined workflow for geographic information systems. In recent years, a large number of flow models were developed following the idea of depth-integration, thereby enlarging the applicability and reliability of this family of process models substantially. It has been previously shown that the Finite Area Method of OpenFOAM<sup>®</sup> can be utilized to express and solve the basic depth-integrated models representing incompressible dense flows. In this manuscript, the previous work (Rauter et al., 2018) is extended beyond the dense flow regime to account for suspended particle flows, such as turbidity currents and powder snow avalanches. A novel coupling mechanism is introduced to enhance the simulation capabilities for mixed snow avalanches. Further, we will give an updated description of the revised computational framework, its integration into OpenFOAM and interfaces to geographic information systems. This work aims to provide practitioners and scientists with an open source tool that facilitates transparency and reproducibility and that can be easily applied to real world scenarios. The tool can be used as a baseline for further developments and in particular allows for modular integration of customized process models.

## 1 Introduction

Run-out and impact simulations of gravitational mass flows typically rely on depth-integrated models (e.g. Pitman et al., 2003; Sampl and Zwinger, 2004; Christen et al., 2010; Iverson and George, 2014; Mergili et al., 2017). In comparison with fully resolved three-dimensional models, this framework provides a range of upsides: The computational expense is substantially reduced, interface and phase tracking are simpler and more reliable, integration in geographic information systems is straightforward. The model is easier to solve numerically, to set up, to calibrate and to evaluate. However, depth-integration comes at a price: The vertical flow structure including the shear gradient is lost and all related effects, if needed for heuristic closures, have to be reintroduced with empirical models. This includes friction, erosion of basal material and its deposition (e.g. Rauter and Köhler, 2020), as well as layering of varying regimes (e.g. Bartelt et al., 2016). A possibility to overcome this is the shallow moment approach (Kowalski and Torrilhon, 2019), however, which has not been applied successfully to real-scenario granular mass flows yet. Nevertheless, depth-integrated models have proven to be a good compromise between simplicity and



25 complexity, especially for flows of **geographic extended** from avalanches (Christen et al., 2010) to tsunamis (Løvholt et al., 2015).

Granular flows show a large variety of behaviours. A very strong distinction of properties can be linked to the Stokes number  **$St$** , expressing the ratio between inertia and drag forces on particles (Boyer et al., 2011; Rauter, 2021). For a flow with shear rate  $\dot{\gamma}$  of granules with density  $\rho_g$  and diameter  $d$ , in a medium of viscosity  $\nu_c$  and density  $\rho_c$ , the Stokes number can be written  
30 as

$$St = d^2 \frac{\dot{\gamma} \rho_g}{\nu_c \rho_c}. \quad (1)$$

At high Stokes numbers, drag forces are small and particles move freely through the surrounding fluid or gas. Thus the bulk motion is dominated by particle-particle interactions and particles will arrange in **a well defined and** relatively high packing density that only depends on the local shear rate and pressure (e.g. Forterre and Pouliquen, 2008). Furthermore, for  
35 many realistic problems, the bulk density can be assumed constant with acceptable accuracy. Dense flow models often take advantage of this fact and are formulated as incompressible non-Newtonian fluids (e.g. Savage and Hutter, 1989; Rauter, 2021).

At low Stokes numbers, drag on particles is substantial and particles are not able to rearrange freely within the carrier medium. Particles and surrounding fluid form a suspension and move like a single fluid, only to be slowly separated by the settling velocity. The **packing density** depends on various aspects and most importantly on the history of the flow. This is a  
40 strong hint that the packing density requires an evolution equation to be properly described (as done by e.g. Parker et al., 1986; Kowalski and McElwaine, 2013; **Bartelt et al., 2016**; **Issler et al., 2018**; Rauter, 2021).

It can be seen from Eq. (1) that the Stokes number depends on the particle size. In polydisperse granular flows, i.e. flows with particles of various sizes (e.g. Barker et al., 2021), this can lead to vertical segregation of small and large particles and thus a coexistence of both regimes. This can be well observed in snow avalanches (**Sovilla et al., 2015**), where a dense flow  
45 is formed by relatively coarse snow blocks of size  $10^{-2}$  m (Rauter et al., 2018) and a powder cloud is formed by small ice particles of size  $10^{-4}$  m (Rastello et al., 2011; Bartelt et al., 2016), see Fig. 1.

In terms of depth-integrated models this calls for a two-layer model, capturing the dense flow with an **incompressible** model and the powder cloud with a suspension model (**Sampl and Zwinger, 2004**; **Bartelt et al., 2016**).

In this work, we will extend the dense flow model of Rauter et al. (2018) to low Stokes number suspension flows following  
50 the model of Parker et al. (1986). We will make and evaluate some adjustments to account for high density differences between the carrier medium and the particles. In a further step, we will combine the models for dense flow and suspension into a two-layer model, capable of simulating mixed snow avalanches, similar to Turnbull and Bartelt (2003) and Bartelt et al. (2016). For this purpose, we have to define a coupling mechanism, i.e. a mass flux term that feeds the powder cloud from the dense core. We develop a novel idealized relation, that encapsulates the essential **relations** of this process and deliberately avoids more  
55 complex mechanisms (e.g. Sampl and Zwinger, 2004; Bartelt et al., 2016). We focus on clarity, simplicity and modularity, and therefore describe all processes with simple, local relations that can be formulated independently of one another. This is motivated by the goal **to get** a simple baseline model but also by the observation that complexity not necessarily leads to better results (Zhao and Kowalski, 2022). The natural terrain is handled as described previously by Rauter et al. (2018). While

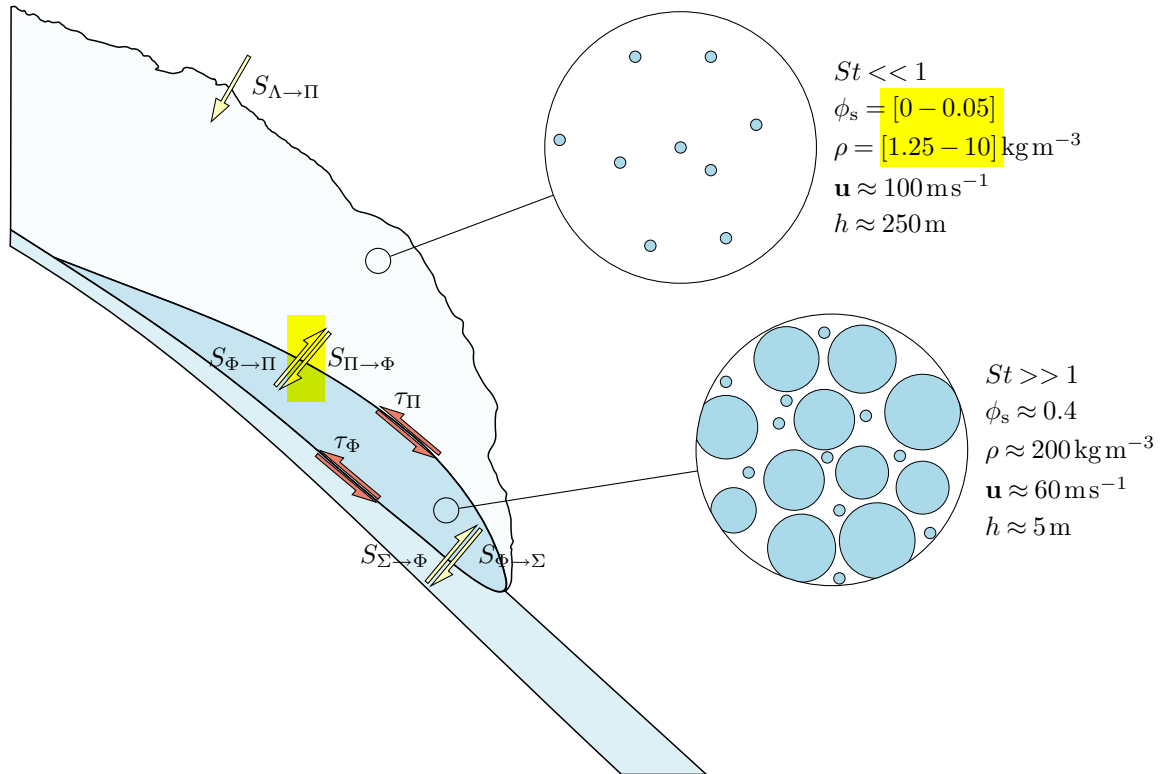


**Figure 1.** Conceptual sketch of a mixed powder snow avalanche, combining an incompressible dense flow of high Stokes number with a variable density suspension cloud characterized by a small Stokes number. The avalanche growth is controlled by the erosion of the intact snow cover and the entrainment of ambient air, the layers are interacting through mass (yellow) and momentum fluxes (red). Characteristic scales of packing density  $\phi_s$ , bulk density  $\rho$ , velocity  $\mathbf{u}$  and height  $h$  vary substantially between layers and thus require individual models.

the main focus of the presented work is snow avalanches, the implementation might very well be useful for the simulation of turbidity currents, as several researchers suspect a dense core in these flows as well (e.g. Heerema et al., 2020).

The **naming convention of layers and fluxes** follows Bartelt et al. (2016), the dense core is denoted with  $\Phi$ , the suspension flow with  $\Pi$ , the static bottom layer with  $\Sigma$  and the stationary ambient fluid with  $\Lambda$ . Flow fields are marked with the respective subscripts and fluxes between layers with two subscripts and an arrow indicating the direction of the flux (see Fig. 1).

The numerical solution and implementation are based on the Finite Area Method (Tuković and Jasak, 2012; Rauter and Tuković, 2018) as implemented in OpenFOAM. Its modular structure and building blocks have proven to be flexible and highly valuable for physical depth-integrated models. Various code parts are reused between all models and various communities, in particular the numerical solver, geometry and data handling but also various **physical code**, such as friction models. Beside the introduction of the new model **and** capabilities, this work **should highlight** the **capability of extending** the basic OpenFOAM solver to complex models.



70 The toolchain to process the basic terrain data, all the way to the final simulation visualisation was improved substantially since the work of Rauter et al. (2018) and many external dependencies were removed, in order to facilitate a tight integration into OpenFOAM. As such, this paper also represents an updated description of the toolchain and practical applications. In this context we will also give a revised introduction into the Finite Area Method and the specific derivations of depth-integration. The model is aimed equally at practitioners, providing a simple mixed snow avalanche model but also to scientists, providing an open model and framework that can be easily modified and extended to evaluate new concepts and ideas.

The novel model is evaluated with various synthetic test cases and finally applied to two real scale events, namely the 1988 Wolfsgruben avalanche and the 2019 Eiskar avalanche.

## 2 Foundation and Framework

### 2.1 Conservation Equations and Depth-integration

80 The presented method fundamentally relies on balance equations, in particular, the conservation of mass and momentum for fluids. The combination of these two equations is widely known as Navier-Stokes Equations (e.g. Ferziger and Peric, 2002) and can be written as

$$\frac{\partial \rho}{\partial t} + \nabla \cdot (\rho \mathbf{u}) = 0, \quad (2)$$

$$\frac{\partial \rho \mathbf{u}}{\partial t} + \nabla \cdot (\rho \mathbf{u} \mathbf{u}) = \nabla \cdot \mathbf{T} + \mathbf{f}, \quad (3)$$

85 with the bulk density  $\rho$  and the bulk velocity  $\mathbf{u}$ . (Note that it can also be defined for an individual phase with some modifications, see, e.g. Rauter, 2021). These flow fields are functions of time  $t$  and space  $\mathbf{x} = (x, y, z)^T$ . The model (2) and (3) describes their evolution from a known state  $\mathbf{u}(0, \mathbf{x}) = \mathbf{u}_0$ ,  $\rho(0, \mathbf{x}) = \rho_0$ , (initial condition) under the influence of boundary conditions. The divergence of the stress tensor  $\mathbf{T}$  acts as diffusion of momentum, the volume force  $\mathbf{f}$  represents additional forces, such as gravitational acceleration.

90 Appropriate closure relations that express the stress tensor  $\mathbf{T}$  as a function of the unknown flow fields yield a well-posed problem that can, in principle, be solved with numerical methods (Barker and Gray, 2017). However, even a well-posed problem is often not practically feasible from a computational perspective. Therefore, multiple simplifications have to be made to make problems of practical relevance accessible. Simplifications often come in the form of averaging over a certain time or over space to get rid of turbulent structures (Reynolds-averaging, see e.g. Ferziger and Peric, 2002), to describe the average behaviour of multiple interpenetrating phases (phase-averaging, e.g. Rauter, 2021) or to get rid of the vertical dimension (e.g. Savage and Hutter, 1989; Rauter and Tuković, 2018). The latter is referred to as depth-averaging or depth-integration and avoids the calculation of three dimensional flow details. It yields mean values of e.g. density  $\bar{\rho}$  and velocity  $\bar{\mathbf{u}}$  along the depth.



In the simplest case, where the depth-integration is aligned with a spatial axis, e.g. the z-axis, the problem can be reduced from three  $(x, y, z)$  to two dimensions  $(x, y)$ . In this case, the depth-averaged value for an arbitrary field  $\psi$  is defined as

$$100 \quad \bar{\psi}(x, y, t) = \frac{1}{h} \int_0^h \psi(x, y, z, t) dz \quad (4)$$

The newly introduced field  $h(x, y, t)$  describes the flow depth, here in terms of the z-coordinate of the top boundary of the integration, for a bottom boundary assumed to be aligned with  $z = 0$ . The bottom and top boundaries are usually defined such that the mass flux through them is zero, meaning that they move with the vertical velocity of the flow at the respective position. The simplest example of such a model are the Shallow Water Equations (Barré de Saint-Venant, 1871). Defining the boundary  
 105 in any other way, will lead to additional source or sink terms, depending on the mass flux through the boundary (Pudasaini and Hutter, 2007). Examples would be any kind of entrainment and deposition fluxes.

Depth-integrated models are often considered synonymous with two-dimensional models. However, real avalanches and landslides travel along paths and surfaces in three-dimensional space. The three-dimensional nature of the terrain has to be reintroduced by modifying the two-dimensional model equations. Most often this is accomplished by abandoning Cartesian  
 110 coordinate systems and Euclidean geometry, which was described in detail first by Savage and Hutter (1989, 1991) and many others in more detail and accuracy since then (e.g. Bouchut and Westdickenberg, 2004; Denlinger and Iverson, 2004; Pudasaini et al., 2005; Hergarten and Robl, 2015). This introduces various correction terms based on Christoffel formalism that are difficult to handle in complex models. In practice, idealized approximations are frequently employed (e.g. in RAMMS, see Fischer et al., 2012), leading to a disparity between theory and practical implementation.

115 An alternative to two-dimensional models with excessive curvature terms is the direct solution of the governing equations in three-dimensional space (Craster and Matar, 2009; Hagemeyer et al., 2011; Rauter and Tuković, 2018). Depth-integration is still compatible with this approach and it can in principle be conducted in any direction pointing out of the surface. Yet in this work, depth-integration is always conducted in direction of the normal vector  $\mathbf{n}^\Gamma$  to the flow surface  $\Gamma$ , as shown in Fig. 2. This has formally to be conducted in a surface-aligned coordinate system  $x'-y'-z'$ ,

$$120 \quad \bar{\psi}(\mathbf{x}_b) = \frac{1}{h} \int_0^h \det(\mathbf{J}) \psi(\mathbf{x}', t) dz' \approx \frac{1}{h} \int_0^h \psi(\mathbf{x}', t) dz'. \quad (5)$$

The Jacobi-matrix  $\mathbf{J}$ , representing the transformation  $\partial \mathbf{x}' / \partial \mathbf{x}$  and its determinant  $\det(\mathbf{J})$  take into account the curvature of the surface and its influence of the volume in a differential volume element of the flow (Bouchut et al., 2003). This effect is of order  $h/R$  (Bouchut et al., 2003) with the mean curvature radius  $R$ , and thus small for mildly curved surfaces ( $R$  is small  
 125 in comparison to the flow height  $h$ ). As in most other models, the influence of the curvature on depth-integration is ignored in this work.

## 2.2 Surface Partial Differential Equations

Depth-integration in terms of Eq. (5) projects all three-dimensional flow fields onto the surface  $\Gamma$  they are constrained by. The conservation equations can then be expressed as surface partial differential equations (SPDEs) that are defined on the surface

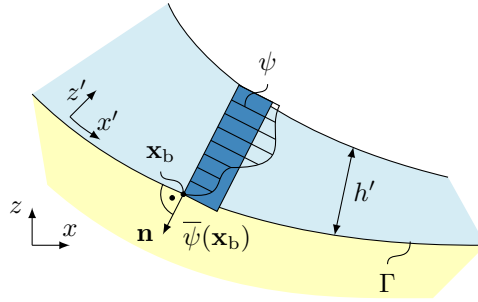


**Figure 2.** Depth integration reduces the full three-dimensional flow field  $\psi$  (dashed area) to an average flow field  $\bar{\psi}$  (blue filled area), that is assigned to a point  $\mathbf{x}_b \in \Gamma$ .

$\Gamma$  and include derivatives of various fields along it. These derivatives are emerging from depth-integrating the ordinary three-dimensional Nabla operator  $\nabla$ . The Nabla operator is a vector of the derivatives in all directions and can be expressed in terms of Cartesian coordinates as

$$\nabla = \left( \frac{\partial}{\partial x}, \frac{\partial}{\partial y}, \frac{\partial}{\partial z} \right)^T. \quad (6)$$

The directional derivative of an arbitrary field  $\psi(\mathbf{x})$ , e.g. in direction of the flow surface normal  $\mathbf{n}^\Gamma$  can be calculated with the scalar product,

$$\frac{\partial \psi}{\partial \mathbf{n}^\Gamma} = \nabla \psi \cdot \mathbf{n}^\Gamma. \quad (7)$$

The surface tangential derivative is consequently obtained by subtracting the derivative in normal direction of the surface (including the respective direction,  $\mathbf{n}^\Gamma$ )

$$\nabla_s^\Gamma \psi = \nabla \psi - (\nabla \psi \cdot \mathbf{n}^\Gamma) \mathbf{n}^\Gamma = (\mathbf{I} - \mathbf{n}^\Gamma \mathbf{n}^{\Gamma T}) \cdot \nabla \psi, \quad (8)$$

with the identity matrix  $\mathbf{I}$  (multiplications of vectors without dot express the outer product  $n_i n_j$ ). The matrix  $\mathbf{P} := \mathbf{I} - \mathbf{n}^\Gamma \mathbf{n}^{\Gamma T}$  hence defines a projection matrix that maps a vector  $\psi$  to the surface's tangential space and constitutes the surface tangential gradient operator (Deckelnick et al., 2005). Per its local definition, the surface tangential derivative does not incorporate local curvature information. The surface gradient with respect to the complex surface topography, however, acknowledges local curvature, and can be written as

$$\nabla^\Gamma \psi = \nabla_s^\Gamma \psi + \kappa \psi \mathbf{n}^\Gamma, \quad (9)$$

in which  $\kappa$  denotes the local Gaussian curvature (Dieter-Kissling et al., 2015; Tuković and Jasak, 2012). Since  $\nabla_s^\Gamma$  projects on the tangential space, it does not contain normal components. As a consequence, the normal directed contribution to  $\nabla^\Gamma \psi$  is solely determined by the curvature term  $\kappa \psi \mathbf{n}^\Gamma$ . By defining  $\nabla_n^\Gamma \psi = \kappa \psi \mathbf{n}^\Gamma (= \mathbf{n}^\Gamma \mathbf{n}^{\Gamma T} \nabla^\Gamma \psi)$  the decomposition into tangential and normal direction reads

$$\nabla^\Gamma \psi = \nabla_s^\Gamma \psi + \nabla_n^\Gamma \psi. \quad (10)$$



150 Following the same rationale, we can compute the surface tangential derivative as

$$\nabla_s^\Gamma = \nabla^\Gamma \cdot (\mathbf{I} - \mathbf{n}^\Gamma \mathbf{n}^\Gamma), \quad (11)$$

and all curvature effects as

$$\nabla_n^\Gamma = \nabla^\Gamma \cdot (\mathbf{n}^\Gamma \mathbf{n}^\Gamma) = \kappa \mathbf{n}^\Gamma, \quad (12)$$

without the requirement to explicitly calculate the curvature. The surface gradient can be easily calculated with Gauss Surface  
 155 Theorem (Dieter-Kissling et al., 2015; Tuković and Jasak, 2012; Rauter and Tuković, 2018).

It remains to be established how the differential operators from three-dimensional models can be depth-integrated. They are, similar to ordinary fields, see Eq. (5), integrated in surface normal direction and **in the surface aligned coordinate system**  
 $x'-y'-z'$ ,

$$\begin{aligned} \overline{\nabla \psi}(\mathbf{x}_b) &= \frac{1}{h} \int_0^h \det(\mathbf{J}) \nabla' \psi(\mathbf{x}') dz' \approx \frac{1}{h} \int_0^h \nabla' \psi(\mathbf{x}') dz' \\ &= \frac{1}{h} \int_0^h \left( \nabla^\Gamma \psi(\mathbf{x}') + \frac{\partial}{\partial z'} \psi(\mathbf{x}') \mathbf{e}'_z \right) dz' \\ &= \frac{1}{h} \int_0^h \nabla^\Gamma \psi(\mathbf{x}') dz' + \frac{1}{h} \int_0^h \frac{\partial}{\partial z'} \psi(\mathbf{x}') dz' \mathbf{e}'_z \\ &= \int_0^h \frac{\nabla^\Gamma \psi(\mathbf{x}')}{h} dz' + \frac{\psi(\mathbf{x}_t) - \psi(\mathbf{x}_b)}{h} \mathbf{n}^\Gamma \\ &= \nabla^\Gamma \overline{\psi}(\mathbf{x}_b) + \frac{\psi(\mathbf{x}_t) - \psi(\mathbf{x}_b)}{h} \mathbf{n}^\Gamma, \end{aligned} \quad (13)$$

where  $\mathbf{x}_b$  is a point on the bottom of the flow (and thus the flow surface  $\Gamma$ ) and  $\mathbf{x}_t$  the corresponding point on the free surface  
 165 of the flow. The second term on the right hand side of Eq. (13) represents an additional sink or source term, that arises if  $\psi$  is not zero at the bottom,  $\mathbf{x}_b$ , or the top of the flow,  $\mathbf{x}_t$ , for example entrainment or basal friction.

Due to the depth-integration in a surface aligned coordinate system, the surface derivative  $\nabla^\Gamma$  appears in the depth-integrated conservation equations. It is decomposed into surface normal and surface tangential components with Eqs. (11) and (12). In the momentum conservation equation, tangential components determine the velocity evolution while surface normal components  
 170 determine the basal pressure. In addition to surface normal components that emerge from curvature effects, there will be normal components appearing due to local sources, such as the gravitational acceleration. In the classical Shallow Water Equations and the Savage and Hutter (1989, 1991) model, this partition is simply achieved by separating the conservation equations in  $x$ - and  $y$ -direction from the equation in  $z$ -direction.

With these building blocks, and some knowledge on how to transform one-dimensional shallow flow models (e.g. Savage  
 175 and Hutter, 1989; Parker et al., 1986), it is possible to extend nearly arbitrary depth-integrated flow models to complex terrain.

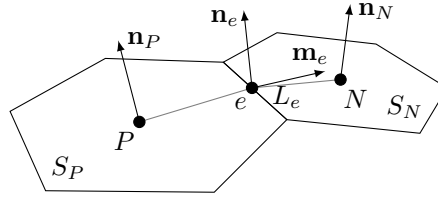


**Figure 3.** A finite area cell  $P$  and its neighbour  $N$ , used to calculate the approximation of surface derivatives in terms of the surface Gauss theorem, integrating fluxes through cell edges  $e$  with length  $L_e$  and outward pointing vector  $\mathbf{m}_e$ .

In particular, ordinary depth-integrated flow models represent the surface tangential momentum conservation equation and the flow depth equation. The two-dimensional  $\nabla$ -operators have to be replaced with the surface tangential  $\nabla_s^\Gamma$ -operators. The surface normal momentum conservation equation can be applied to replace the usually simplified expression for the basal pressure.

### 180 2.3 Finite Area Method

Partial Differential Equations, as well as their SPDE counterparts, are rarely solvable in an analytical sense, especially practical problems that represent real world situations (Ferziger and Peric, 2002). Therefore, we rely on numerical approximations of SPDEs and the Finite Area Method. This method is a variation of the Finite Volume Method (see Ferziger and Peric, 2002; Jasak, 1996; Moukalled et al., 2016, for details) in  $N + 1$  dimensions, where  $N$  is the dimension of the control volumes. This means that for two-dimensional control volumes (i.e. surfaces), vectorial entities, such as normal vectors, velocities or fluxes, will be three-dimensional. Similar to the conventional Finite Volume Method, the Gaussian Surface Theorem (Tuković and Jasak, 2012) is applied and discretized by simplifying a control surface  $S$  as a flat, convex polygon  $S_i$ , as shown in Fig. 3. The expressions for the differential operators follow as

$$\nabla^\Gamma \psi = \frac{1}{S} \oint_{\partial S} \mathbf{m}^\Gamma \cdot \psi \, dL \approx \frac{1}{S_i} \sum \psi_e \mathbf{m}_e L_e \quad (14)$$

190 and

$$\nabla^\Gamma \cdot \psi = \frac{1}{S} \oint_{\partial S} \mathbf{m}^\Gamma \cdot \psi \, dL \approx \frac{1}{S_i} \sum \psi_e \cdot \mathbf{m}_e L_e. \quad (15)$$

Index  $e$  refers to a discrete number of straight edges that form the polygon with surface  $S_i$ .  $\psi_e$  is the average value of the field  $\psi$  on the edge  $e$ ,  $L_e$  its length and  $\mathbf{m}_e$  the  $\Gamma$ -tangential and edge-normal outward pointing vector.  $S_i$ ,  $L_e$  and  $\mathbf{m}_e$  are purely geometrical properties that are defined during mesh generation. Values of fields on edges  $\psi_e$ , on the other hand, are interpolated from values of edge-adjacent cells,  $\psi_P$  and  $\psi_N$ . This introduces flux transport across cells and represents the flow of mass or information from one cell to neighbouring ones. The fluxes can then be associated in a linear system of equations that is solved with a suitable method.





Discretization of non-gradient terms, e.g. the temporal derivative or any source term, is done in complete analogy to the Finite Volume Method and obtained from integration over the control surface  $S_i$ . For details we refer to the large amount of excellent literature on the Finite Volume Method (Ferziger and Peric, 2002; Jasak, 1996; Moukalled et al., 2016; LeVeque, 2002).

### 3 Dense Flow Model

The dense flow model describes the flow of incompressible material with density  $\rho_\Phi$  (see Fig. 1). In case of a granular mass flow, the density follows from the grain density  $\rho_g$  and the volumetric packing density  $\phi_\Phi$  as

$$\rho_\Phi = \phi_\Phi \rho_g. \quad (16)$$

However, fluids can be simulated with this model as well, in which case  $\rho_\Phi$  is the intrinsic density of the fluid. The depth-integrated mass and momentum conservation equations follow as

$$\frac{\partial h_\Phi}{\partial t} + \nabla^\Gamma \cdot (h_\Phi \bar{\mathbf{u}}_\Phi) = \frac{S_\Phi^\phi}{\phi_\Phi}, \quad (17)$$

$$\frac{\partial h_\Phi \bar{\mathbf{u}}_\Phi}{\partial t} + \xi_\Phi \nabla_s^\Gamma \cdot (h_\Phi \bar{\mathbf{u}}_\Phi \bar{\mathbf{u}}_\Phi) = -\frac{\boldsymbol{\tau}_\Phi}{\rho_\Phi} + h_\Phi \mathbf{g}_s - \frac{1}{2\rho_\Phi} \nabla_s^\Gamma (h_\Phi p_\Phi) + \frac{S_\Phi^u}{\rho_\Phi}, \quad (18)$$

$$\xi_\Phi \nabla_n^\Gamma \cdot (h_\Phi \bar{\mathbf{u}}_\Phi \bar{\mathbf{u}}_\Phi) = h_\Phi \mathbf{g}_n - \frac{1}{2\rho_\Phi} \nabla_n^\Gamma (h_\Phi p_\Phi) - \frac{1}{\rho_\Phi} \mathbf{n}^\Gamma p_\Phi. \quad (19)$$

The unknown flow fields are the flow depth  $h_\Phi$ , the depth-integrated velocity  $\bar{\mathbf{u}}_\Phi$  and the basal pressure  $p_\Phi$ . The gravitational acceleration is represented by its surface tangential projection  $\mathbf{g}_s = (\mathbf{I} - \mathbf{n}^\Gamma \mathbf{n}^\Gamma) \mathbf{g}$  and its surface normal projection  $\mathbf{g}_n = (\mathbf{n}^\Gamma \mathbf{n}^\Gamma) \mathbf{g}$ . Equation (19) represents the surface normal component of the momentum conservation equation and yields the basal pressure  $p_\Phi$ .

The factor  $\xi_\Phi$  denotes the shape factor that compensates for errors introduced by switching integration and multiplication, namely  $\xi_\Phi \bar{\mathbf{u}}_\Phi \bar{\mathbf{u}}_\Phi = \overline{\mathbf{u}_\Phi \mathbf{u}_\Phi}$ . It depends on the velocity profile and as such on the constitutive model and the state of the flow. It is usually neglected or set to a theoretical and constant value, derived e.g. from the Bagnold (1954) velocity profile ( $\xi_\Phi = 5/4$ ).

#### 3.1 Friction in the Dense Flow Model

The term  $\boldsymbol{\tau}_\Phi$  represents the depth-integrated divergence of the shear stress tensor and thus the constitutive model of the flowing mass. Assuming that the top boundary is stress free and that surface tangential derivatives of the deviatoric stress tensor are small, the only remaining entity is the basal friction. In this work, we will use the friction model presented by Rauter et al. (2016), which is closely related to the widely used Voellmy (1955) friction model. It is given as

$$\boldsymbol{\tau}_\Phi = \left( \mu p_\Phi + \frac{\rho_\Phi |\mathbf{g}|}{\chi h_\Phi^2} |\bar{\mathbf{u}}_\Phi|^2 \right) \frac{\bar{\mathbf{u}}_\Phi}{|\bar{\mathbf{u}}_\Phi|}, \quad (20)$$

with dry friction coefficient  $\mu$  and turbulent friction coefficient  $\chi$ . A wide range of alternative friction models can be found in the literature and a number of them are implemented into the presented software.



### 3.2 Entrainment and Deposition in the Dense Flow Model

$S_{\Phi}^{\phi}$  represents the sum of all volumetric source and sink terms of grains, e.g. erosion and entrainment of additional mass or its deposition,  $S_{\Phi}^u$  represents its associated momentum. Dividing by the packing density in Eq. (17) simplifies handling of density changes in the different flow regimes. In the simplest case, e.g. laboratory experiments on **inclined planes or chutes**, the source and sink terms are zero.

For snow avalanches and many other realistic gravitational mass flows, entrainment of erodible material along the avalanche path plays an important role. A popular entrainment model can be derived by comparing the dissipated energy in the mass flow with the energy required to mobilize the static material (Fischer et al., 2015),

$$S_{\Sigma \rightarrow \Phi}^{\phi} = \frac{\tau_{\Phi} \cdot \bar{u}_{\Phi}}{\rho_{\Phi} e_b} \phi_{\Phi}, \quad (21)$$

with the specific erosion energy  $e_b$  as the single parameter. Here it is assumed that the packing density of the static layer is the same as in the dense flow  $\phi_{\Phi}$ .

Rauter and Köhler (2020) presented an extension to account for the deposition of flowing material,  $S_{\Phi \rightarrow \Sigma}^{\phi}$ . This aspect is neglected in this work and the flow height of the last time step is assumed to be the final deposition of the model.

The total flux term between the static layer and the flowing avalanche is determined as the difference between entrainment and deposition,

$$S_{\Phi}^{\phi} = S_{\Sigma \rightarrow \Phi}^{\phi} - S_{\Phi \rightarrow \Sigma}^{\phi}. \quad (22)$$

The related momentum source and sink terms are zero in the case of single layer flows, as both erodible and deposited material is static.

The height (in **surface normal** direction) of the static material on the topography can be tracked with an additional evolution equation,

$$\frac{\partial h_{\Sigma}}{\partial t} = \frac{S_{\Sigma}^{\phi}}{\phi_{\Phi}}, \quad (23)$$

with

$$S_{\Sigma}^{\phi} = S_{\Phi \rightarrow \Sigma}^{\phi} - S_{\Sigma \rightarrow \Phi}^{\phi}, \quad (24)$$

again under the assumption that the static layer has the same packing density as the flowing avalanche  $\phi_{\Phi}$ . Tracking the thickness of the static layer allows to limit the available entrainable material, hence to turn **off** entrainment if the erodible layer is depleted.

## 4 Suspension Flow Model

The suspension flow model describes the flow of a dynamic mixture of a granular material of density  $\rho_g$  and the surrounding fluid of density  $\rho_c$ . It corresponds, to some degree, to a depth-integration of the compressible model of Rauter (2021). The



255 mixture density follows as

$$\rho_{\Pi} = \phi_{\Pi} \rho_g + (1 - \phi_{\Pi}) \rho_c, \quad (25)$$

with the variable packing density or phase fraction  $\phi_{\Pi}$ . Introducing the **buoyancy** density ratio,

$$r = \frac{\rho_g - \rho_c}{\rho_c}, \quad (26)$$

the mixture density can be expressed as

$$260 \quad \rho_{\Pi} = \rho_c (1 + \phi_{\Pi} r). \quad (27)$$

The **buoyancy assumption**, an often applied simplification (e.g. Parker et al., 1986), implies that  $\phi_{\Pi} \lesssim 10^{-2}$  and  $r \approx 1$  and thus  $\rho_{\Pi} \approx \rho_c$ . This is reasonable if  $\rho_g$  and  $\rho_c$  are at least similar in order of magnitude, e.g. sand in water. However, this does not **hold for snow avalanches**, i.e. mixtures of grains or ice ( $\rho_g \approx 1000 \text{ kg m}^{-3}$ ) with air ( $\rho_c \approx 1 \text{ kg m}^{-3}$ ). Thus, we will omit this assumption and consider the dynamic density as given by Eq. (27) in all terms.

265 Due to the variable mixture, there will be two phases that have to be described by balance laws. In depth-averaged frameworks, this is usually handled by describing the total volume occupied by the flowing masses (grains and flowing ambient fluid) in terms of the flow depth  $h_{\Pi}$  and the volume of grains, expressed by the depth-integrated volume fraction  $h_{\Pi} \bar{\phi}_{\Pi}$  (Parker et al., 1986; Bartelt et al., 2016; Kowalski and McElwaine, 2013). The phases are assumed to move with the same velocity  $\bar{\mathbf{u}}_{\Pi}$ , differences in velocity (e.g. settling of particles) are considered with empirical corrections.

270 The depth-integrated **mass** and momentum conservation equations follow as

$$\frac{\partial h_{\Pi}}{\partial t} + \nabla^{\Gamma} \cdot (h_{\Pi} \bar{\mathbf{u}}_{\Pi}) = S_{\Pi}^h, \quad (28)$$

$$\frac{\partial \bar{\phi}_{\Pi} h_{\Pi}}{\partial t} + \nabla^{\Gamma} \cdot (\bar{\phi}_{\Pi} h_{\Pi} \bar{\mathbf{u}}_{\Pi}) = S_{\Pi}^{\phi}, \quad (29)$$

$$\frac{\partial (1 + r \bar{\phi}_{\Pi}) h_{\Pi} \bar{\mathbf{u}}_{\Pi}}{\partial t} + \xi_{\Pi} \nabla_s^{\Gamma} \cdot ((1 + r \bar{\phi}_{\Pi}) h_{\Pi} \bar{\mathbf{u}}_{\Pi} \bar{\mathbf{u}}_{\Pi}) = -\frac{\tau_{\Pi}}{\rho_c} + r \bar{\phi}_{\Pi} h_{\Pi} \mathbf{g}_s - \frac{1}{2} \nabla_s^{\Gamma} \cdot ((1 + r \bar{\phi}_{\Pi}) g_{\text{eff}} h_{\Pi}^2) + \frac{S_{\Pi}^{\text{su}}}{\rho_c}. \quad (30)$$

All equations and terms are well known from the dense flow model, except for the additional **tracking of grains** with Eq. (29).

275 The unknown flow fields are the flow depth  $h_{\Pi}$ , the depth-averaged velocity  $\bar{\mathbf{u}}_{\Pi}$  and the depth-averaged phase fraction or packing density  $\bar{\phi}_{\Pi}$ . Assuming  $r \bar{\phi}_{\Pi} \approx 0$  in all terms but the gravitational acceleration (buoyancy assumption), leads to the popular model of Parker et al. (1986). Removing the surface tangential gravitational acceleration leads to the momentum conservation equation of Bartelt et al. (2016). The effective gravitational acceleration  $g_{\text{eff}}$  is the surface normal gravitational acceleration, corrected for centripetal acceleration due to curved terrain. In terms of surface partial differential equations, it can  
 280 be easily expressed as (see appendix A)

$$g_{\text{eff}} \approx \mathbf{n}^{\Gamma} \cdot \left( \mathbf{g} - \nabla^{\Gamma} \cdot (\bar{\mathbf{u}}_{\Pi} \bar{\mathbf{u}}_{\Pi}) \right). \quad (31)$$

This expression replaces the rather complex calculation of the basal pressure in the dense flow model. It is justified here, as the basal pressure has only a weak influence on the flow dynamics of the suspended flow. Further, this notation turns out to



be convenient later, as various internal processes in the suspension flow are depending on effective gravity. A particle on a  
285 streamline of the flow, will approximately experience a volume force corresponding to this acceleration and processes like the  
terminal settling velocity will depend on this adjusted value.

Considerable attention has to be drawn to the volumetric source and sink terms,  $S_{\Pi}^h$  and  $S_{\Pi}^{\phi}$  and the associated momentum  
flux  $S_{\Pi}^u$ . These terms are responsible for the varying flow height and the depth-averaged **packing density** and influence the flow  
dynamics substantially.

#### 290 4.1 Friction in the Suspension Flow Model

Similar as in the dense flow model, the term  $\tau_{\Pi}$  represents the depth-integrated divergence of the shear stress tensor. If the  
particle fraction in the suspension is low, it can be treated as a simple fluid. Assuming **laminar** flow, the friction can be calculated  
with a constant wall friction coefficient  $c_D$  (Parker et al., 1986),

$$\tau_{\Pi} = \rho_c c_D |\bar{\mathbf{u}}_{\Pi}| \bar{\mathbf{u}}_{\Pi}. \quad (32)$$

295 However, suspension flows are inherently turbulent, reaching Reynolds numbers of up to  $10^9$  (Meiburg et al., 2015), as they  
**need to pick up particles and keep them suspended**. Nevertheless we will use the simple laminar model in this work. Under  
turbulent conditions, the wall friction coefficient  $c_D$  loses its physical meaning and takes the form of an empirical parameter  
that might require adaption to flow conditions. Further, it is assumed that all dissipative processes, such as inter-granular  
friction (e.g. Boyer et al., 2011), are included in this term. Considering the accuracy and uncertainties of the problems at hand,  
300 this seems to be a reasonable compromise. Alternative approaches are the turbulent friction model of Parker et al. (1986), a  
depth-integration of the Einstein viscosity model (e.g. Boyer et al., 2011) or a more complex granular rheology (Boyer et al.,  
2011).

#### 4.2 Ambient fluid entrainment in the Suspension Flow Model

The volume of the suspension flow will grow due to entrainment of ambient fluid. It is assumed (Parker et al., 1986; Turner,  
305 1986; Ancy, 2004) that ambient fluid entrainment depends solely on the **Richardson** number, which is given as

$$Ri_{\Pi} = \frac{r g_{\text{eff}} \bar{\phi}_{\Pi} h_{\Pi}}{\bar{\mathbf{u}}_{\Pi}^2}. \quad (33)$$

In contrast to e.g. Parker et al. (1986), we use the effective surface **normal** acceleration  $g_{\text{eff}}$  instead of the constant gravitational  
acceleration  $|g|$  to account for the influence of centripetal forces on particles in the flow. Adjusting the Richardson number  
with the centripetal acceleration leads to an increased amount of ambient fluid entrainment if the flow runs over convex terrain  
310 and to a decreased amount if the flow runs over concave terrain.

There are various models for the relation between the Richardson number and the entrainment. Parker et al. (1986) use a  
simple, inverse proportional approach,

$$S_{\Lambda \rightarrow \Pi}^h = |\bar{\mathbf{u}}_{\Pi}| \frac{\alpha}{Ri_0 + Ri_{\Pi}}, \quad (34)$$

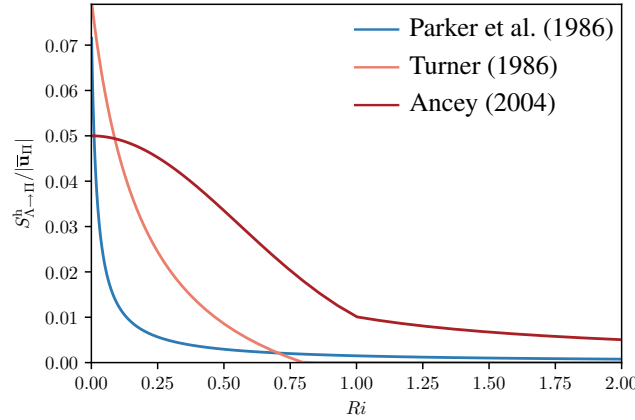


**Figure 4.** Comparison of the air entrainment functions, all depending solely on the Richardson number  $Ri$ .

with the parameters  $\alpha = 0.00153$  and  $Ri_0 = 0.204$ .

315 Turner (1986) provides an alternative formulation

$$S_{\Lambda \rightarrow \Pi}^h = |\bar{u}_{\Pi}| \begin{cases} \frac{Ri_0 - Ri_{\Pi}}{\alpha_1 + \alpha_2 Ri_{\Pi}} & \text{for } Ri_{\Pi} < Ri_0, \\ 0 & \text{for } Ri_{\Pi} \geq Ri_0. \end{cases} \quad (35)$$

with the parameters  $Ri_0 = 0.8$ ,  $\alpha_1 = 10$  and  $\alpha_2 = 50$ . Various different parameters were suggested for this empirical relation, see e.g. Ancey (2004).

320 Finally, Ancey (2004) suggested yet another relation in form of an exponential function, here given in the form of Issler et al. (2018)

$$S_{\Lambda \rightarrow \Pi}^h = |\bar{u}_{\Pi}| \alpha_2 \begin{cases} \exp(-\alpha_1 Ri^2) & \text{for } Ri_{\Pi} < 1, \\ \exp(-\alpha_1)/Ri & \text{for } Ri_{\Pi} \geq 1. \end{cases} \quad (36)$$

The parameter  $\alpha_1$  is supposed to be the only free parameter, with a value of 1.6 following Issler et al. (2018), however, due to different definitions of the entrainment rate an additional parameter  $\alpha_2$  is required. In order to be of similar magnitude as the other air entrainment relations,  $\alpha_2$  has to be roughly 0.05. All relations are shown in Fig. 4.

### 325 4.3 Grain entrainment and settlement in the Suspension Flow Model

Suspension flows are, similar to dense flows, able to erode granular material from the bed. It is, in principle, possible to use the same entrainment relations as in the dense flow model, but specialized entrainment relations have been proposed in literature.



An example for **subaquatic** turbidity currents, is given by Parker et al. (1986) as

$$S_{\Sigma \rightarrow \Pi}^{\phi} = v_s \begin{cases} 0.3 & \text{for } Z > Z_m, \\ 3 \cdot 10^{-12} Z^{10} \left(1 - \frac{Z_c}{Z}\right) & \text{for } Z_c < Z < Z_m, \\ 0 & \text{for } Z < Z_c, \end{cases} \quad (37)$$

330 with

$$Z = Re_g \frac{\sqrt{\tau_{\Pi}}}{v_s}, \quad (38)$$

the settling velocity

$$v_s = \frac{r g_{\text{eff}} d_{\Pi}^2}{18 \nu_c}, \quad (39)$$

the particles Reynolds number

$$335 \quad Re_g = \frac{\sqrt{r g_{\text{eff}} d_{\Pi}} d_{\Pi}}{\nu_c}, \quad (40)$$

the viscosity of the ambient fluid  $\nu_c$  and two empirical parameters  $Z_m = 13.2$  and  $Z_c$ . The parameter  $Z_c$  was reported to be approximately 5, we found that a value of exactly 0.5 is required to reproduce the examples of Parker et al. (1986) in the examples shown in section 7.2.

The settling of grains is given by Parker et al. (1986) as

$$340 \quad S_{\Pi \rightarrow \Sigma}^{\phi} = v_s r_0 \phi_{\Pi}, \quad (41)$$

with the settling velocity as given in Eq. (39) and the factor  $r_0$  for the bottom value of the grain concentration

$$r_0 = 1 + 31.5 \left( \sqrt{\frac{\tau_{\Pi}}{\rho_c}} \frac{1}{v_s} \right)^{-1.46}. \quad (42)$$

As before, the total flux term follows as the difference between entrainment and deposition,

$$S_{\Pi}^{\phi} = S_{\Sigma \rightarrow \Pi}^{\phi} - S_{\Pi \rightarrow \Sigma}^{\phi}. \quad (43)$$

345 The momentum flux into the suspension due to ambient fluid and grain entrainment is zero. The volume occupied by entrained and deposited grains and the respective flux term in the evolution equation of the flow height  $h_{\Pi}$  is neglected at this point.

## 5 Two-layer Granular Flow Model

Granular mass flows can show different regimes, especially in terms of the Stokes number. Sampl and Zwinger (2004) and others (Jóhannesson et al., 2009) describe three regimes, the dense flow, transition or re-suspension and powder snow layer, 350 Sovilla et al. (2015) recognize five regions in mixed snow avalanches and Köhler et al. (2018) identified seven regimes. Here we



aim to represent the two limit cases of dense flow and suspension in a single model, similar to Bartelt et al. (2016). It is assumed that these regimes are described in appropriate accuracy either by the Savage and Hutter (1989, 1991) model, Equations (17) to (19), or the Parker et al. (1986) model, Equations (28) to (30). The layers will communicate with mass fluxes  $S^\phi$  or  $S^h$  and momentum fluxes  $S^u$ . In particular, the fluxes of grains are (see also Fig. 1) for the static layer (deposition of the dense flow model is neglected),

$$S_\Sigma^\phi = S_{\Phi \rightarrow \Sigma}^\phi - S_{\Sigma \rightarrow \Phi}^\phi, \quad (44)$$

for the dense flow layer

$$S_\Phi^\phi = S_{\Sigma \rightarrow \Phi}^\phi - S_{\Phi \rightarrow \Sigma}^\phi + S_{\Pi \rightarrow \Phi}^\phi - S_{\Phi \rightarrow \Pi}^\phi, \quad (45)$$

and for the suspension layer

$$S_\Pi^\phi = S_{\Phi \rightarrow \Pi}^\phi - S_{\Pi \rightarrow \Phi}^\phi. \quad (46)$$

Entrainment from the suspension layer is assumed to be negligible small in comparison to the overall mass fluxes and thus not explicitly accounted for in the simulations. The term  $S_{\Phi \rightarrow \Pi}^\phi$  describes the upward mass flux from the dense flow to the suspension flow. It is the remaining term to be specified in the following (see section 5.1). The flux in the opposite direction  $S_{\Pi \rightarrow \Phi}^\phi$  is assumed to be equal to the settling flux of the suspension layer  $S_{\Pi \rightarrow \Sigma}^\phi$ , i.e. the deposition from the suspension is redirected to the dense core and further to the static layer from there, if the deposition model of the dense flow model is active. The corresponding momentum fluxes for the dense flow layer and the suspension layer are

$$S_\Phi^u = -S_\Pi^u = \bar{u}_\Pi S_{\Pi \rightarrow \Phi}^\phi - \xi_{t\Phi} \bar{u}_\Phi S_{\Phi \rightarrow \Pi}^\phi, \quad (47)$$

accounting for the momentum that is transferred together with grains between moving layers. The shape factor  $\xi_t$  takes into account that the velocity at the top boundary of the avalanche, where particles are tossed into the suspension layer, is higher than the depth-integrated velocity. It is related to the previously shown shape factor and can similarly be calculated on basis of e.g. the Bagnold (1954) velocity profile as  $5/3$ . The particles that fall from the suspension layer onto the dense flow layer,  $S_{\Pi \rightarrow \Phi}^\phi$ , are assumed to carry the velocity of the suspension layer. The momentum fluxes from and to the static layer are zero due to the respective velocity at the interface.

Further we have to account for the volume of fluid that is pushed into the suspension layer with particles. Assuming that particles enter at a packing density of  $\phi_{0\Pi}$ , we have to add a source term of the form

$$S_{\Phi \rightarrow \Pi}^h = \phi_{0\Pi} S_{\Phi \rightarrow \Pi}^\phi. \quad (48)$$

The value  $\phi_{0\Pi}$  is set to the phase fraction of the dense core in this work. This avoids unreasonably high grain fractions if a suspension flow is initiated by a dense flow avalanche.

In addition to the momentum fluxes, that are related to the mass fluxes, we need to consider the shear stress on the interface. This relation is chosen to be identical to the basal shear stress of the suspension layer,  $\tau_\Pi$ , however, it is no longer proportional



to the velocity of the suspension layer, but to the relative velocity between the dense flow and the suspension layer,

$$\tau_{\Pi} = \rho_c c_D |\bar{\mathbf{u}}_{\Pi} - \bar{\mathbf{u}}_{\Phi}| (\bar{\mathbf{u}}_{\Pi} - \bar{\mathbf{u}}_{\Phi}). \quad (49)$$

In areas where the suspension layer detaches from the dense flow, the dense flow velocity is assumed to be zero and the model collapses to the friction model of the ordinary suspension model. An equal but opposite stress term to  $\tau_{\Pi}$  should be applied to the dense core to account for the friction of the top surface of the dense core. However, it is assumed that this stress is already included in the empirical formulation and parametrisation of  $\tau_{\Phi}$ , because the top surface friction is also present in pure dense snow avalanches with a stationary or moving air layer above it. The ambient fluid entrainment of the suspension layer stays unchanged.

The mass flux  $S_{\Phi \rightarrow \Pi}^{\phi}$  feeds the suspension layer from the dense core and the associated momentum flux, in combination with the shape factor propels the suspension flow forwards. This is assumed to be the mayor genesis mechanism for the suspension cloud, similar to Bartelt et al. (2016).

## 5.1 Cross-layer coupling

All fluxes of the two layer model are described relatively well in literature (see sections above), except for the mass flux from the dense flow layer to the suspension layer,  $S_{\Phi \rightarrow \Pi}^{\phi}$ , for which only few suggestions can be found (Sampl and Zwinger, 2004; Bartelt et al., 2016). Existing relations do conceptually not fit into the presented framework, either due to missing granular mechanics (Sampl and Zwinger, 2004) or due to their dependence on a specific dense flow model (Bartelt et al., 2016). For the purpose of introducing this framework we choose a simple relation, based on local flow fields of the dense flow.

We assume that the dense flow is composed of small and large particles with diameter  $d_{\Pi}$  and  $d_{\Phi}$ , respectively. Uptake of particles into the suspension layer requires small particles to be made available by the dense layer that mostly consists of large particles (Bartelt et al., 2016), and the capability of the suspension layer to keep them suspended. The latter is already implemented into the model in form of the settling model of the suspension flow  $S_{\Pi \rightarrow \Phi}^{\phi}$ . This term is depending on the Reynolds particle number  $Re_g$  which is similar to the Stokes number and a good indicator for the flow regime.

The first step, making small particles available to the suspension, is assumed to be triggered by a fluidized flow that is expanding in volume, sucking in air and increasing the distance between particles. There are various hints on how this expression should look like. At first it is useful to look at dimensionless properties in the dense flow. Beside the non-dimensional volumetric mass flux  $S_{\Phi \rightarrow \Pi}^{\phi}/|\bar{\mathbf{u}}_{\Phi}|$ , these are (Forterre and Pouliquen, 2008; Rauter, 2021) the friction coefficient  $\mu_{\Phi} = |\tau_{\Phi}|/p_{\Phi}$ , the packing density  $\phi_{\Phi}$  and the inertial number

$$I_{\Phi} = \frac{d_{\Phi} \dot{\gamma}_{\Phi}}{\sqrt{p_{\Phi}/\rho_g}}, \quad (50)$$

with the shear rate at the bottom of the dense flow (Bagnold, 1954)

$$\dot{\gamma}_{\Phi} = \frac{4}{3} \frac{|\bar{\mathbf{u}}_{\Phi}|}{h_{\Phi}}. \quad (51)$$





It is well established that  $\mu_\Phi$  and  $\phi_\Phi$  can be expressed as a function of only the inertial number  $I_\Phi$  and it is reasonable to assume that fluidisation can be described the same way. This is further emphasized by the linear relationship between the packing density and the inertial number in the dense flow regime (Forterre and Pouliquen, 2008). Finally, Rauter et al. (2016) found a specific relation between the shear rate  $\dot{\gamma}_\Phi$  and the pressure  $p_\Phi$  in a granular kinetic theory model (Vescovi et al., 2013) at the point where fluidisation suddenly occurs,

$$\frac{\dot{\gamma}_\Phi}{p_\Phi^{0.37}} = \text{const.} \quad (52)$$

Comparing this relation to the expression for the inertial number, one can observe a striking resemblance, solely the exponent of the pressure is slightly lower in the relation of Rauter et al. (2016). This strongly indicates that the mass flux from the dense flow to the suspension can be expressed as a function of the inertial number only, starting at a minimum value  $I_0$  and growing with a specified rate  $s_f$  from thereon

$$\frac{S_{\Phi \rightarrow \Pi}^\phi}{|\mathbf{u}_\Phi|} (I_\Phi) = \max(I_\Phi - I_0, 0) s_f. \quad (53)$$

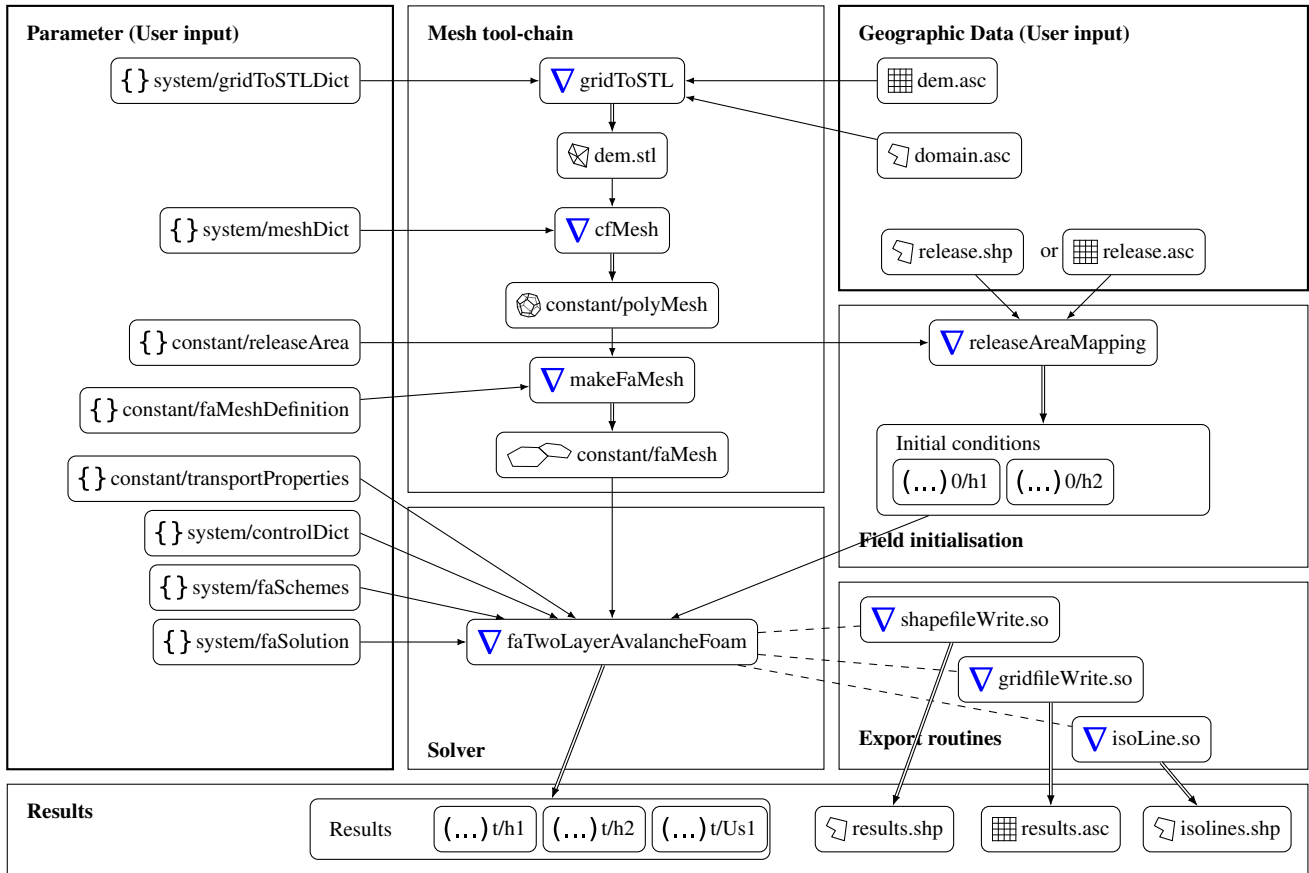
The results of Rauter et al. (2016) suggest that the value of  $I_0$  is close to 0.5, as at this point explosive fluidisation starts to occur. The factor  $s_f$  is expected to be small, as the vertical velocity has to be substantially smaller than the flow velocity. This parameter can be optimized to yield the correct relation between dense flow and powder cloud.

In this model, small particles will be made available to the suspension when the dense flow velocity is high or when the pressure is low, e.g. when an avalanche is running over a bump. If the small particles are sufficiently small, the suspension will be able to keep the particles suspended and a powder cloud will form. Otherwise, the particles will fall back to be reintegrated by the dense core, expressed by the deposition mass flux of the suspension layer, which is stronger for larger particles. The parameters for the suggested model are the small and large particle diameters  $d_\Pi$  and  $d_\Phi$ , the minimum value of  $I$  at which fluidisation occurs  $I_0$ , the particle density  $\rho_g$  and the factor  $s_f$ . All parameter except for the latter are already used in the model or known otherwise.

Relation (53) finally completes the model and closes the system that will be solved numerically in the following. The model could be improved by tracking and limiting the availability of small particles or by making this property temperature-dependent.

## 6 Pre- and Postprocessing

The pre- and postprocessing of simulations with the presented models follows the workflow depicted by Rauter et al. (2018). The capabilities of respective tools have been improved and fully implemented in C++ to allow a seamless integration into OpenFOAM and computational clusters that do not support Python and some of the previously used libraries. Most improvements are based on a native implementation of two common geographic information system (GIS) data types, ESRI® shape files and ESRI® grid files. The native implementation allows all solvers and utilities of the OpenFOAM avalanche module to directly read and write from or to the respective files. This enables many previously difficult tasks that are presented in the following. Generally, all tools are steered with text files that follow the usual OpenFOAM syntax, called dictionary (see Fig. 5).



**Legend:**

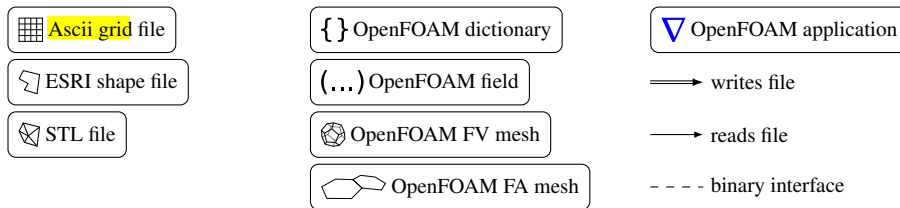


**Figure 5.** Pipeline of the OpenFOAM avalanche module. The pipeline has been simplified substantially since the work of Rauter et al. (2018). Most notably, all components are fully implemented in C++ and included into the module. The pipeline includes the complete workflow, starting from GIS data and returning all results to GIS data. The user can modify parameters in the respective dictionaries and geometry of the simulation domain and the initial conditions in the geographic input data. The solver can be replaced with any of the three models.

This toolchain-based workflow follows the concept of OpenFOAM, which has proven to enable reproducibility, reusability but also rapid development.



## 6.1 Mesh Generation from Terrain Data

445 The mesh generation follows the principles from Rauter et al. (2018). In a first step a triangulation of the terrain and a boundary of the surrounding volume is generated. A new tool for this task, called `gridToSTL`, was written entirely in C++ and without any external dependencies. The tool requires input in form of a polygon that defines the simulation domain and the terrain data in form of a raster file. Other than in the previous version, the polygon can be any kind of closed and non-intersecting polygon with an arbitrary number of edges, either convex or concave. This enables flexibility on the simulation domain, which turned out to be especially useful to cover long and windy submarine canyons.

450 The finite volume mesh is generated from the triangulated surface with an arbitrary mesh generator. This toolchain can not only be applied to the depth-integrated models presented here but was also used for the full three-dimensional model presented by Rauter et al. (2022). In this study we used the mesh generator `pMesh`, while Rauter et al. (2022) used `cartesianMesh`, both of the `cfMesh` toolbox (Juretić, 2015). The finite area mesh is then generated on a dedicated surface of the finite volume mesh using the tool `makeFaMesh`, part of the OpenFOAM finite area module.

## 6.2 Mapping Initial Conditions

Initial conditions can be set with the tool `releaseAreaMapping`. In addition to the functionality of previous versions, this tool is now able to read shape files and grid files and map them directly onto finite area fields to be used by any solver. All input for the tool is read from a dictionary, where further references to shape and grid files can be listed. This tool enables efficient adaptations to new scenarios.

## 6.3 Simulation Run

Once the mesh and the initial conditions are defined, the solver of choice can be run. Currently there are three solvers available in the `avalanche` module, the dense flow solver `faSavageHutterFoam`, the suspension flow solver `faParkerFukushimaFoam` and the mixed flow solver `faTwoLayerAvalancheFoam` (Fig. 5 shows `faTwoLayerAvalancheFoam` only, but it can be replaced with any other model). Physical parameters are read from the file `transportProperties`, general simulation settings are read from the `controlDict` and numerical algorithms and parameters from the files `faSolution` and `faSchemes`. To run the solver in parallel, the tool `decomposePar` has to be run before the solver and the tool `reconstructPar` has to be run after the solver. In the common OpenFOAM manner, all steps for a simulation are listed in a script file named `Allrun`, which can be executed by the user to automatically execute the here proposed pipeline. Another script, named `Allclean` can be run to clean up the simulation directory.

## 6.4 Postprocessing and Data Export

The OpenFOAM architecture allows to execute customized code, called function objects, in every simulation step. Various function objects are made available in the `avalanche` module. Most importantly, this includes function objects to export simulation results as either shape or raster files. The export as shape files can be done cell-wise (one polygon for each computational



475 cell) or the numerical data can be recombined to generate **iso lines** that are written into the shape file. Function objects can be loaded by placing the respective entry in the control dictionary. As of version v2312, all solvers are able to run in a post-processing mode, in which old results are read from hard disc and the function objects are executed. This allows to execute function objects in a post-processing workflow without rerunning the whole simulation.

## 7 Results and Discussion

### 480 7.1 Dense Flow Model

The dense flow model **was** applied to various cases in multiple studies. The interested reader is referred to **Rauter and Tuković** (2018) for lab scale simulations, Rauter et al. (2018) and Huber et al. (2018) for large scale snow avalanche simulations, Rauter and Köhler (2020) for simulations with the deposition model and to Shimizu (2022) for an application to pyroclastic flows.

### 7.2 Suspension Flow Model

485 Parker et al. (1986) simulate steady suspension flows on constantly inclined one-dimensional slopes with the model presented in section 4. Four cases with uniform model parameters but different boundary conditions give a good overview over the behaviour of the model and a verification (as defined by Roache, 1997, **as solving the equations right**) of the presented implementation. The four simulations are conducted on one-dimensional slopes with a gradient of 5%, the gravitational acceleration follows as  $\mathbf{g} = (0.49, 0, -9.81)^T \text{ m s}^{-2}$  (chosen to match the setup by Parker et al., 1986). The parameters suggest that the suspensions  
490 are composed of sediment in water on a scale of a small turbidity current.

Material parameters for this setup are given in Tab. 1. The left boundary condition (at  $x = 0$ ) prescribes the inflow in terms of the height  $h_{\Pi}$ , velocity  $\bar{\mathbf{u}}_{\Pi}$  and grain flux  $\bar{\psi}_{\Pi} = h_{\Pi} \bar{\phi}_{\Pi} \bar{\mathbf{u}}_{\Pi}$ , in particular as shown in Tab. 2. All parameters are given normalized to reference values  $H = 2 \text{ m}$ ,  $U = 0.874 \text{ m s}^{-1}$  and  $\Psi = 0.00828 \text{ m}^2 \text{ s}^{-1}$ .

The right boundary condition is modelled as zero gradient for all fields, mimicking an outlet boundary condition. For a basic  
495 verification of the novel implementation of the suspension model, the respective simulations are repeated and compared to the original results. We will evaluate the buoyancy assumption of Parker et al. (1986), as well as the formulation with the correct density given in here. The simulations are conducted in an unsteady manner until the flow reaches a steady state, comparable to the results reported by Parker et al. (1986). Figure 6 shows results for the four cases.

The first case, starting with a high velocity but low particle fraction increases its particle fraction quickly, as the high velocity  
500 is sufficient to erode and pick up sediment. The second case starts with a very high phase fraction, leading to a sudden ignition of the flow at  $x/H = 60$ . The height of the suspension stays low and even decreases, showing that a high phase fraction can keep the suspension concentrated at the bottom. The third and fourth case start with a low velocity and low particle phase fraction, respectively, and the suspension fades out quickly. The height of the flow is increasing in both cases where the flow is fading out, indicating that the momentum of the flow is diffused over larger volumes of fluid. This is consistent with the  
505 expected scaling of fluid entrainment with the Richardson number.



**Table 1.** Parameters for the **small scale** simulations of Parker et al. (1986).

sub model	parameter	description	value
flow model:		<b>Parker–Fukushima</b>	
	$\rho_s$	density of solid phase (particles)	$2650 \text{ kg m}^{-3}$
	$\rho_c$	density of fluid phase (water)	$1000 \text{ kg m}^{-3}$
	$r$	density ratio, follows as	1.65
	$\nu_c$	viscosity of fluid phase (water)	$10^{-6} \text{ m}^2 \text{ s}^{-1}$
	$d_{\Pi}$	particle diameter	$10^{-4} \text{ m}$
basal friction:		<b>laminar flow</b>	
	$c_D$	drag coefficient	0.004
particle entrainment:		<b>Parker–Fukushima</b>	
	$Z_c$	empirical parameter	0.5
	$Z_m$	empirical parameter	13.2
ambient fluid entrainment:		<b>Parker–Fukushima</b>	
	$Ri_0$	reference Richardson number	0.0204
	$\alpha$	reference ambient fluid entrainment	0.00153
deposition:		<b>Parker–Fukushima</b>	(no parameters)

**Table 2.** Inlet boundary conditions for the small scale simulations of Parker et al. (1986), simulating four scenarios of igniting or fading turbidity currents.

case	$h_{\Pi}/H$	$\bar{u}_{\Pi}/U$	$\bar{\psi}_{\Pi}/\Psi$
(a)	1.0	1.3	0.2
(b)	1.0	0.9	1.7
(c)	1.0	0.7	1.2
(d)	1.0	1.0	0.2

It can be seen that results of Parker et al. (1986) are reproduced with only small **derivations**. The OpenFOAM solver yields sharper edges than the **the** implementation of Parker et al. (1986), especially visible in Fig. 6b. This small difference is most likely **attributed** to the numerical solution method or the numerical resolution. The correction of the time derivative and advection term with  $(1 + r \bar{\phi}_{\Pi})$  has only a minimal influence on the model results. This is reasonable, considering the low value for the buoyant density **ration**  $r = 1.65$  in these cases. These simulations **provide a strong indicator** that the model of Parker et al. (1986) **was** implemented correctly, however, this can not be seen as a validation (Roache, 1997) of the model.

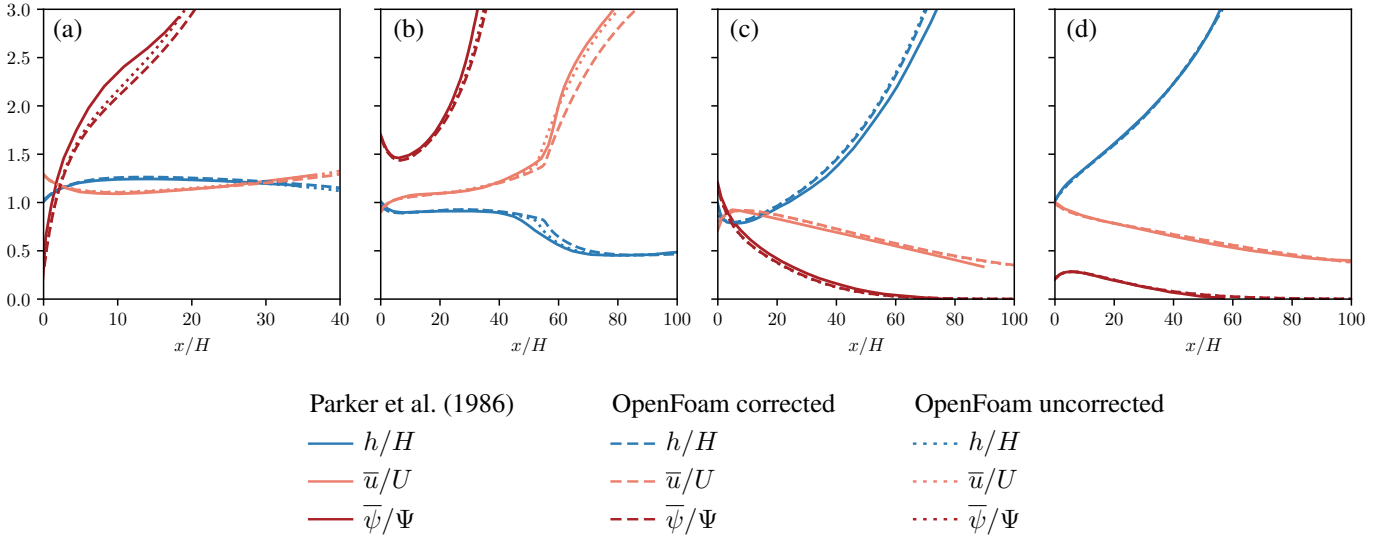


**Figure 6.** Numerical simulation of the four test cases presented by Parker et al. (1986) with OpenFOAM, with and without the buoyancy assumption (corrected and uncorrected, respectively). The results of Parker et al. (1986) are reproduced with good accuracy. The buoyancy assumption fits well to the conditions of these numerical experiments.

### 7.3 Two Layer Model

#### 7.3.1 Synthetic tests and sensitivity study

In order to better understand the **two layer dense flow - suspension flow** model, we **will conduct** tests on synthetic topographies. The topography is based on a parabola with a length  $L = 4000$  m and a height  $H = 2000$  m, with an additional flat runout area of 2000 m. The slope has a width of 2000 m, leading to a simulated region of  $x = [-4000, 2000]$  m and  $y = [-1000, 1000]$  m. In addition, the influence of topographic structures will be investigated, as terrain features often initialize the formation of suspension flows, e.g. powder snow avalanches. A bump in the surface is created by superposing the parabola with a secans hyperbolicus  $\text{sech}(x) = 2/(\exp(x) + \exp(-x))$  at  $X_p = -2700$  m with height  $H_p = 150$  m and length  $L_p = 200$  m,

$$z = H_p \text{sech}\left(\frac{x - X_p}{L_p}\right) + \begin{cases} H \left(\frac{x}{L}\right)^2 & \text{for } x < 0, \\ 0 & \text{otherwise,} \end{cases} \quad (54)$$

inspired by the experiments of Viroulet et al. (2017). All boundaries are implemented as **Neumann** (zero gradient) boundary conditions.

The release area (initial condition) of the slide was **formed by** a square between  $x = [-3900, -3500]$  m and  $y = [-500, 500]$  m and an initial dense flow height of  $h_\phi = 5$  m within that square. All other flow fields are set to zero. The parameters, **roughly** corresponding to snow avalanches are given in Tab. 3, if not mentioned otherwise. The value for the coupling factor  $s_f$  is varied

and the sensitivity of the model to this parameter is investigated. Entrainment and deposition from and to the static layer are not included in this section for simplicity. The simulations were run for 90s.

Beside the flow thickness, velocity and phase fraction, we can analyse the dynamic pressure, which is an important indicator for the destructive potential of the flow. It is defined as

530 
$$p_{d\Phi} = \rho_{\Phi} |\bar{\mathbf{u}}_{\Phi}|^2 \quad (55)$$

for the dense flow and as

$$p_{d\Pi} = (\rho_g \phi_{\Pi} + \rho_c (1 - \phi_{\Pi})) |\bar{\mathbf{u}}_{\Pi}|^2 \quad (56)$$

for the powder cloud (e.g. Jóhannesson et al., 2009). In particular we evaluate the dynamic peak pressure, which the maximum of the dynamic pressure at a fixed point over time. Important limits that are used in the definition of hazard zones, e.g. in Austria, are 1 kPa (yellow zone) and 10 kPa (red zone) (Jóhannesson et al., 2009). Notably, the shape factor should be applied to the dynamic pressure for consistency, increasing all simulated pressures by 25%. However, this is neglected in order to be consistent with previous works and the definition of hazard zones.

Results for a simple parabola (without surface bump) are shown in Fig. 7 for three values of  $s_f$  ( $10^{-5}$ ,  $10^{-4}$ ,  $10^{-3}$ ). This set of simulations allows some valuable conclusions on the model and in particular the coupling model. All simulations start with a dense flow that eventually feeds the powder cloud. The feed of the powder cloud varies strongly due to the variation of the respective parameter  $s_f$ .

For a low value of  $s_f$  the dense flow is not able to generate a strong powder cloud with a considerable phase fraction and thus density. A suspension flow develops eventually, however, it consists almost entirely of air, without any ice particles. Basically, this can be seen as a layer of air that is dragged along by the dense flow. The velocity, dynamic pressure and runout distance of this layer are respectively low. As shown before, the flow height of the suspension layer grows strongly for fading flows, indicating a strong diffusion of momentum.

Increasing the value for  $s_f$  up to  $10^{-4}$  leads to higher phase fractions up to 0.004, roughly corresponding to a density of  $4\text{kg m}^{-3}$ . Further increasing the value to  $10^{-3}$  leads to phase fractions of up to 0.02 and densities of  $20\text{kg m}^{-3}$ , however only for short periods. Notably, these are depth-averaged phase fractions and densities and the respective values close to the surface might be considerably higher. The respective dynamic pressure of the powder cloud is still low and only the simulation with the highest coupling factor  $s_f$  is able to generate a red zone that extends beyond the red zone of the dense flow. These results seem reasonable, considering the relatively low average slope gradient of 50% and the absence of any topographic features that might enhance the feed of the powder cloud. More powerful powder snow avalanches can be expected on steeper slopes and on slopes with high topography variations, e.g. steep cliffs or rough terrain. Further simulations (not shown here) revealed that the powder cloud increases substantially with higher slope gradients.

Results for the slope with a bump are shown in Fig. 8. The model shows a high sensitivity to the terrain and this case represents natural slopes with varying gradients better. All simulations create a considerable powder clouds with high phase fractions. The highest phase fraction is reached shortly after the top of the bump where the negative centrifugal forces are



**Table 3.** Parameters for the two-layer model for synthetic cases on parabolas and for the Wolfsgruben and Eiskar avalanches.

sub model	parameter	description	parabola	Wolfsgrube	Eiskar
	$\rho_s$	Density of solid phase (snow/ice)	$800 \text{ kg m}^{-3}$	$800 \text{ kg m}^{-3}$	$800 \text{ kg m}^{-3}$
	$\rho_c$	Density of fluid phase (air)	$1.25 \text{ kg m}^{-3}$	$1.25 \text{ kg m}^{-3}$	$1.25 \text{ kg m}^{-3}$
	$\nu_c$	Viscosity of fluid phase (air)	$1.5 \cdot 10^{-5} \text{ m}^2 \text{ s}^{-1}$	$1.5 \cdot 10^{-5} \text{ m}^2 \text{ s}^{-1}$	$1.5 \cdot 10^{-5} \text{ m}^2 \text{ s}^{-1}$
dense flow:		<b>Savage–Hutter model</b>			
	$\phi_\Phi$	Packing density in the dense flow	0.25	0.25	0.25
	$d_\Phi$	large particle diameter	$10^{-2} \text{ m}$	$10^{-2} \text{ m}$	$10^{-2} \text{ m}$
	$\xi_\Phi$	Shape factor	1.25	1.25	1.25
	$\xi_{t\Phi}$	shape factor for velocity at top	1.67	1.67	1.67
dense flow friction:		<b>Simplified Kinetic Theory</b>			
	$\mu$	Dry friction coefficient	0.25	0.26	0.20
	$\chi$	dynamic friction coefficient	$10^4 \text{ m}^{-1} \text{ s}^{-2}$	$8700 \text{ m}^{-1} \text{ s}^{-2}$	$10^4 \text{ m}^{-1} \text{ s}^{-2}$
dense flow entrainment:		<b>Erosion energy</b>			
	$e_b$	Erosion energy		$10^3 \text{ m}^2 \text{ s}^{-2}$	$10^3 \text{ m}^2 \text{ s}^{-2}$
powder cloud:		<b>Parker–Fukushima model</b>			
	$d_{II}$	small particle diameter	$10^{-4} \text{ m}$	$10^{-4} \text{ m}$	$10^{-4} \text{ m}$
	$\xi_{II}$	shape factor	1.25	1.25	1.25
powder cloud friction:		<b>Laminar flow</b>			
	$c_D$	drag coefficient	0.5	0.5	0.1
ambient fluid entrainment:		<b>Parker–Fukushima</b>			
	$Ri_0$	reference Richardson number	0.0204	0.0204	0.0204
	$\alpha$	reference air entrainment factor	0.00153	0.00153	0.00153
powder cloud deposition:		<b>Parker–Fukushima</b> (no parameters)			
coupling:		<b>Inertial number scaling</b>			
	$I_0$	reference inertial number	0.5	0.5	0.5
	$s_f$	reference suspension feed factor	$10^{-5}$	$10^{-5}$	$10^{-4}$

strongest and the basal pressure the lowest. The phase fraction reaches up to 0.05, roughly corresponding to a density of  
 560  $50 \text{ kg m}^{-3}$ . A shock is formed at the bump in the suspension layer due to the high gradient in the phase fraction, leading to a  
 considerable pressure gradient that decelerates the flow. In all simulations the dynamic powder cloud pressure exceeds 10 kPa  
 and the respective high pressure zone extends beyond the dense flow runout. The 1 kPa zone of the powder cloud reaches  
 considerable runouts beyond the dense flow.

The results on synthetic terrain show a reasonable behaviour of the model, both in terms of parametrisation and response  
 565 to the terrain. The effect of the terrain is well visible and corresponds to the assumptions from which the model was derived.  
 The sensitivity of the model to the parameter  $s_f$  is well pronounced and this factor can be utilized to fit the model to real world  
 observations. A value between  $10^{-4}$  and  $10^{-5}$  seems reasonable for the parameter of the coupling model.



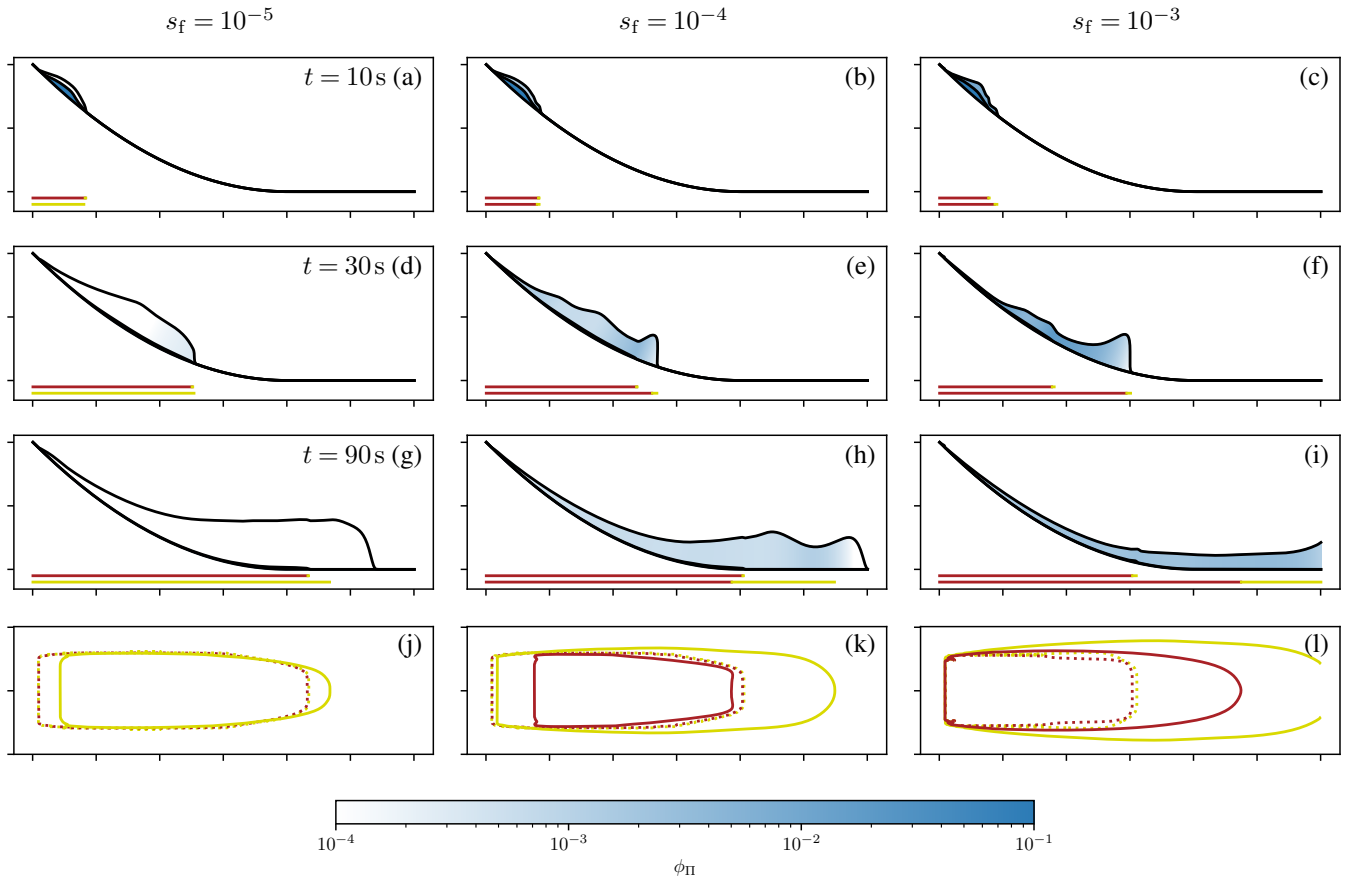


**Figure 7.** Numerical simulations of **snow** avalanches on a parabolic slope with the two layer model. The parameter  $s_f$  was varied between  $10^{-5}$  (a,d,g,j),  $10^{-4}$  (b,e,h,k) and  $10^{-3}$  (c,f,i,l). Panels (a)-(i) show the cross section in the middle of the slide. The slope is shown as the lower black line. The flow thickness  $h_\phi$  is shown as offset from the surface magnified by a factor of 20, the flow thickness  $h_\pi$  is shown above the dense flow magnified by a factor of 10. The powder cloud is coloured according to the phase fraction  $\phi_\pi$ . The red and yellow lines below the slope mark the regions of high dynamic peak pressure  $p_d > 10$  kPa and intermediate dynamic pressure  $p_d > 1$  kPa for the dense flow (top) and the powder cloud (bottom) respectively. Panels (j)-(l) show the regions of high and intermediate dynamic peak pressure (dashed: dense flow, continuous: powder cloud) from the top. One tick on the axis equals 1000 m.

Finally, we **will use** synthetic cases to showcase the sensitivity of the model to the air entrainment. Figure 9 shows the simulation on the synthetic terrain with the three presented air entrainment models. The differences are small but noticeable. In particular, the entrainment is stronger with the model of Ancey (2004), **however, which is just a question of parametrisation.** More importantly, the model of Turner (1986) shows a more pronounced flow head. The Richardson number is low in the head and the relation of Turner (1986) predicts the strongest entrainment at low Richardson numbers, see Fig. 4. Generally, all relations appear reasonable and well in line with each other. We will continue with the entrainment model of Parker et al.

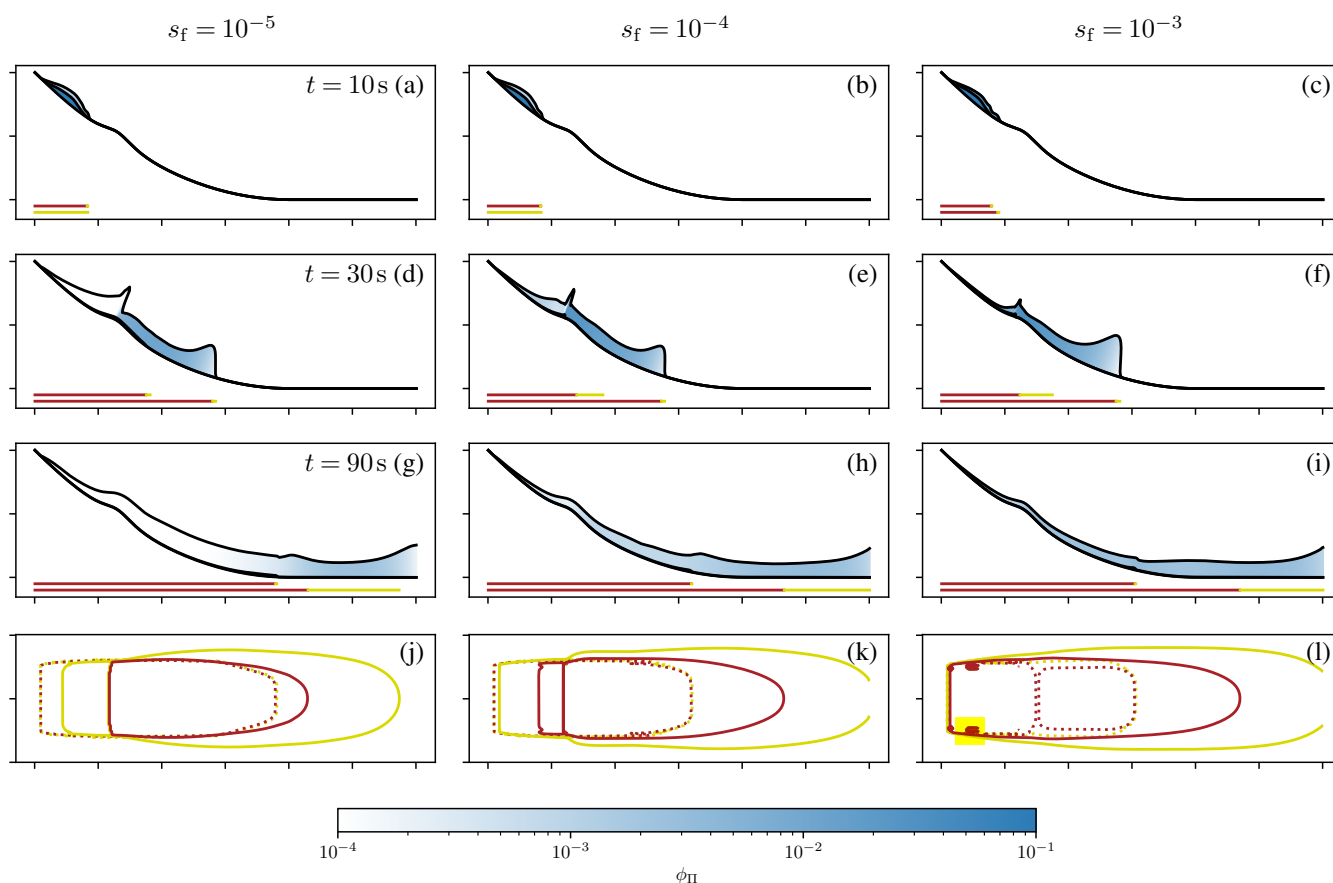


**Figure 8.** Numerical simulations of snow avalanches on a parabolic slope with a bump with the two layer model. Same as Fig. 7 but with a bump with height 150 m and length 200 m at  $x = -2700$  m.

(1986) from here on. Considering an optimisation of air entrainment parameters to real events, it might be useful to apply the  
 575 model of Ancey (2004) instead, as it provides the clearest parametrisation.

### 7.3.2 Real case example: The 1988 Wolfsgruben Avalanche

The 1988 Wolfsgruben Avalanche represents an important event in Austria, as it was the trigger for many developments and  
 used repeatedly as a benchmark. The event, or at least its dense core, was featured by Fischer et al. (2015) and Rauter et al.  
 (2018). Here we revisit the event with the new two layer model and include the powder cloud into the analysis. The avalanche  
 580 is characterized by a channelised, steep slope with an angle of  $30^\circ$  that transitions quickly into the flat valley floor and the  
 opposite slope.

The preprocessing and simulation setup follows Rauter et al. (2018) but with the novel tool-chain and an extended simulation  
 domain to cover the full runout of the powder cloud. The initial release area of the avalanche and the erodible snow covers are

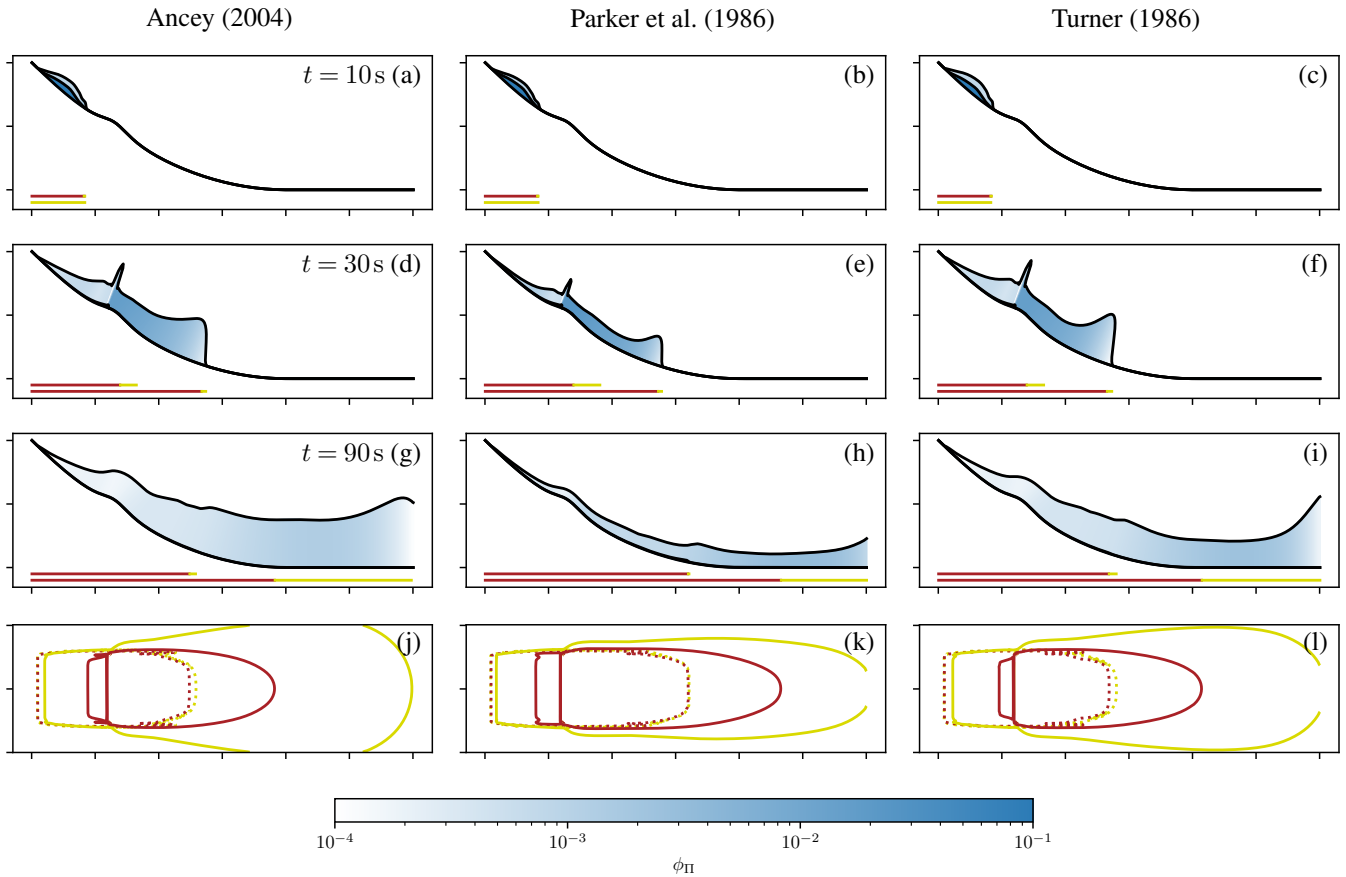


**Figure 9.** Numerical simulations of snow avalanches on a parabolic slope with a bump. Same as Fig. 8 but with a variation of the air entrainment model and a fixed parameter  $s_f$ .

the same, following the linear approach

$$585 \quad h_{\Sigma}|_{t=0}(z) = \left( h_{\Sigma}(z_0) + \frac{\partial h_{\Sigma}}{\partial z}(z - z_0) \right) \cos(\theta), \quad (57)$$

where  $z$  is the surface elevation and  $z_0$  the elevation of a reference point with the base value  $h_{\Sigma}(z_0)$ . The growth rate  $\frac{\partial h_{\Sigma}}{\partial z}$  defines the **evolution** from that point.  $\theta$  is the angle between the gravitational acceleration and the surface-normal vector. For the 1988 Wolfsgruben Avalanche we use the snow cover parameters  $h_{\Sigma}(z_0) = 1.61$  m,  $z_0 = 1289$  m,  $\frac{\partial h_{\Sigma}}{\partial z} = 8 \cdot 10^{-4}$ .

The model parameters are shown in Tab. 3. The dense flow parameters have been optimized in a previous study (Fischer  
 590 et al., 2015) and although we use a slightly different friction model, **the parameters fit the case well**. The suspension parameters are deduced from literature where possible (density, grain diameter). The coupling parameter  $s_f = 10^{-5}$  was found after running some simulations, starting from the values derived from the simulations on synthetic cases. A higher value **lead** to an unrealistically short dense flow runout, a lower value to a severe underestimation of the suspension impact pressure. The



friction coefficient  $c_D$  was chosen sufficiently large for the powder cloud to **not completely decouple from the dense core**.  
595 Apart from this effect, the simulation is rather insensitive to the friction coefficient  $c_D$ .

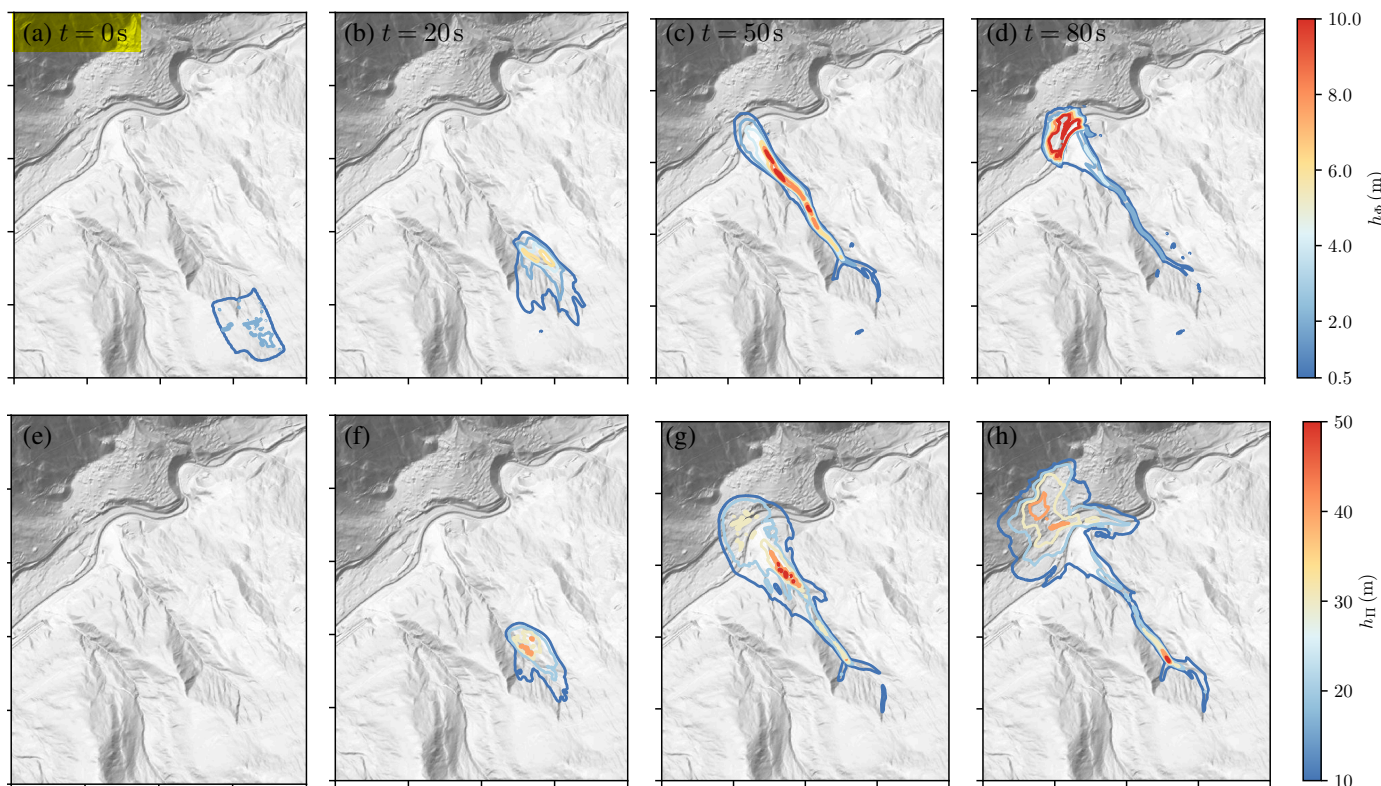


**Figure 10.** Numerical simulation of the Wolfsgruben avalanche with the two layer model. The first row (a-d) shows the height of the dense flow layer, the second row (e-h) shows the height of the powder cloud layer. Each tick on the x- and y-axes corresponds to 500 m.

Four time steps of the simulation are shown in Fig. 10, displaying **isolines** of the dense flow height  $h_\Phi$  (a-d) and the suspension flow height  $h_\Pi$  (e-h). The avalanche starts as a dense flow and rapidly accelerates due to the steep release area (Fig. 10a). Shortly after the release a strong suspension layer is formed that further accelerates beyond the velocity of the dense flow layer (Fig. 10b,f). After roughly 40 – 50s the avalanche reaches the bottom of the valley (Fig. 10c,g). The powder cloud outruns the dense flow and hits the valley floor first. The dense flow is stopped quickly due to the high granular friction while the powder cloud keeps running up on the opposite slope for approximately 50 m of elevation. Both flows experience a shock that increases the flow height in the valley floor drastically. The deposition, i.e. the dense flow height in the last time step, reaches up to 15 m, however, which does not account for the difference between flow ( $\approx 200 \text{ kg m}^{-3}$ ) and deposition density ( $\approx 600 \text{ kg m}^{-3}$ ).

605 Results for the dense flow can be validated by a comparison with the deposition (see Fig. 11b) **and** they are similar to previous studies with the same model and the model SamosAT (Fischer et al., 2015; Rauter et al., 2018). Results for the powder cloud

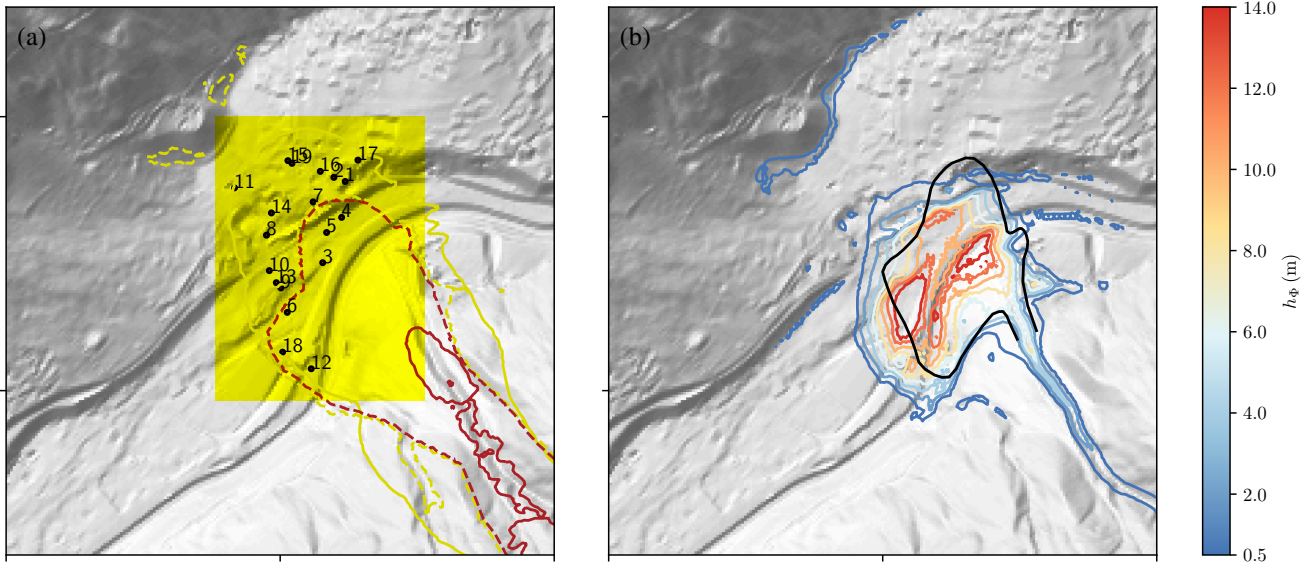


**Figure 11.** (a) The dynamic peak pressure of the suspension layer (solid lines) and the dense flow layer (dashed line). The yellow line marks the 1 kPa isoline and the red line the 10 kPa isoline. (b) The deposition of the avalanche (at  $t = 180$  s).

are more difficult to validate. Traces of the powder cloud that can be identified in the field are limited and not **straight forward** to interpret, **as no clear deposition pattern emerges from suspended flows**. Further, the respective deposition can hardly be related to the impact pressure and thus the destructive potential of the flow. Therefore, we compare the simulated dynamic pressure with observed building damages from the respective avalanche (see Fig. 11a). This includes not only the suspension layer but also the dense flow. An evaluation of the dynamic peak pressure and the deposition height at damaged objects is shown in Tab. 4.

The dense flow does not reach the two destroyed buildings (Point 1 and 2 in Fig. 11a and Tab. 4) **and stops** about 20 m short. Points 12 and 18 were only slightly damaged by the suspension flow in reality but severely hit by the dense flow in the simulation, showing that the simulation tends too strongly to the left side (viewed **in flow direction**). The deposition height that was recorded at selected points (Tab. 4) is matched well, assuming a compaction of the avalanche by a factor of 3 after deposition.

The suspension layer shows a very limited zone of high dynamic pressure ( $> 10$  kPa) but an extended zone of **intermittent** dynamic pressure (1 – 10 kPa). The model predicts dynamic pressures of 1 – 4 kPa where balconies and roofs have been damaged and 1 – 3 kPa where windows have been destroyed. This corresponds well with engineering estimations of resistance capabilities of the respective parts: Windows are assumed to break at 2 – 4 kPa, doors, walls and roofs at 3 – 6 kPa (Sovilla et al., 2015). The dynamic pressure of the suspension layer at the destroyed buildings (Point 1 and 2 in Fig. 11) is not sufficient to destroy the respective brick structures (25–45 kPa). These high values strongly indicate that the dense flow or an **intermittent** regime must be responsible for these high impact pressures (see pictures in Fischer et al., 2015). Therefore, we conclude that



**Table 4.** Simulated dynamic peak pressure at the location where damage was observed.

Number	$h_{\Phi}$	$p_{d\Phi}$	$p_{d\Pi}$	Observed damage
1	0.2 m	0 kPa	3.1 kPa	Destroyed house (dense flow > 10 kPa)
2	0.2 m	0 kPa	2.6 kPa	Destroyed house (dense flow > 10 kPa)
3	12.5 m	71.9 kPa	5.1 kPa	Large deposition (4.0 m)
4	12.2 m	73.1 kPa	4.1 kPa	Large deposition (3.5 m)
5	11.3 m	72.5 kPa	4.3 kPa	Large deposition (2.5 m)
6	12.3 m	13.1 kPa	2.1 kPa	Large deposition (1.8 m)
7	2 m	0 kPa	4.2 kPa	Damaged roof and balcony (> 1 kPa)
8	0.5 m	0 kPa	2.3 kPa	Damaged balcony (> 1 kPa)
9	5.3 m	1.1 kPa	2.3 kPa	Damaged roof (> 1 kPa)
10	2 m	0 kPa	1.9 kPa	Damaged roof (> 1 kPa)
11	0.4 m	0 kPa	0.9 kPa	Damaged roof and windows (> 1 kPa)
12	11.2 m	29.4 kPa	1.7 kPa	Damaged windows (> 1 kPa)
13	3.7 m	0.8 kPa	1.9 kPa	Damaged windows (> 1 kPa)
14	0.7 m	0 kPa	2.5 kPa	Damaged windows (> 1 kPa)
15	0.3 m	0 kPa	2 kPa	Damaged windows (> 1 kPa)
16	0.2 m	0 kPa	2.8 kPa	Damaged windows (> 1 kPa)
17	0.2 m	0 kPa	1.4 kPa	Damaged windows (> 1 kPa)
18	6.8 m	16.7 kPa	1.3 kPa	Delimbed tree
19	0.2 m	0 kPa	2.4 kPa	Delimbed tree

625 the simulated suspension layer reaches all observed traces of the powder cloud without covering the region where no traces  
 could be observed.

### 7.3.3 Real case example: The 2019 Eiskar Avalanche

On 15<sup>th</sup> of January 2019, the Eiskar avalanche was released after intense snow falls and a quick temperature drop (Oesterle,  
 2019). The topography of the Eiskar avalanche differs drastically from the Wolfsgruben avalanche and thus provides a good  
 630 supplement to that case. The avalanche was initiated by a collapsing slab on the right hand side of the avalanche path (looking  
 in flow direction) and was falling on a larger snow field. From there, the avalanche slope continues with an inclination of  
 approximately 25° for 1500 m until reaching a flatter slope of 10°. The dense flow avalanche ran 1000 m on the flat slope  
 and the powder flow exceeded the dense flow by another 500 m, reaching the village of Ramsau. The powder cloud destroyed  
 a wooden building, damaged a hotel and knocked over a bus. The dynamic pressure required for the damage was estimated  
 635 at 1 – 3 kPa. Areal pictures were taken after the event, which allowed to estimate the initial snow cover, the release area and  
 deposition. The data was used to derive parameters for the snow cover function (Eq. (57)),  $h_{\Sigma}(z_0) = 1.60$  m,  $z_0 = 1275$  m,  
 $\frac{\partial h_{\Sigma}}{\partial z} = 2 \cdot 10^{-3}$  to reach a snow cover thickness of approximately 2.7 m at an elevation of 2200 m (Oesterle, 2019). Other  
 aspects of the simulation, such as the preparation of the terrain data match the simulation of the Wolfsgruben avalanche.





640 The first simulation (not shown) was conducted with the same parameters as for the Wolfsgruben avalanche. However, these parameters lead to a severe underestimation of the powder cloud, running short by approximately 400m. Simulations with the model SamosAT (Sampl and Zwinger, 2004) showed similar results with the standard parameters (Oesterle, 2019). Therefore the friction coefficients and the coefficient for the suspension feed were adjusted (see Tab. 3) to reach an appropriate runout and dynamic pressure at the observed impacts.

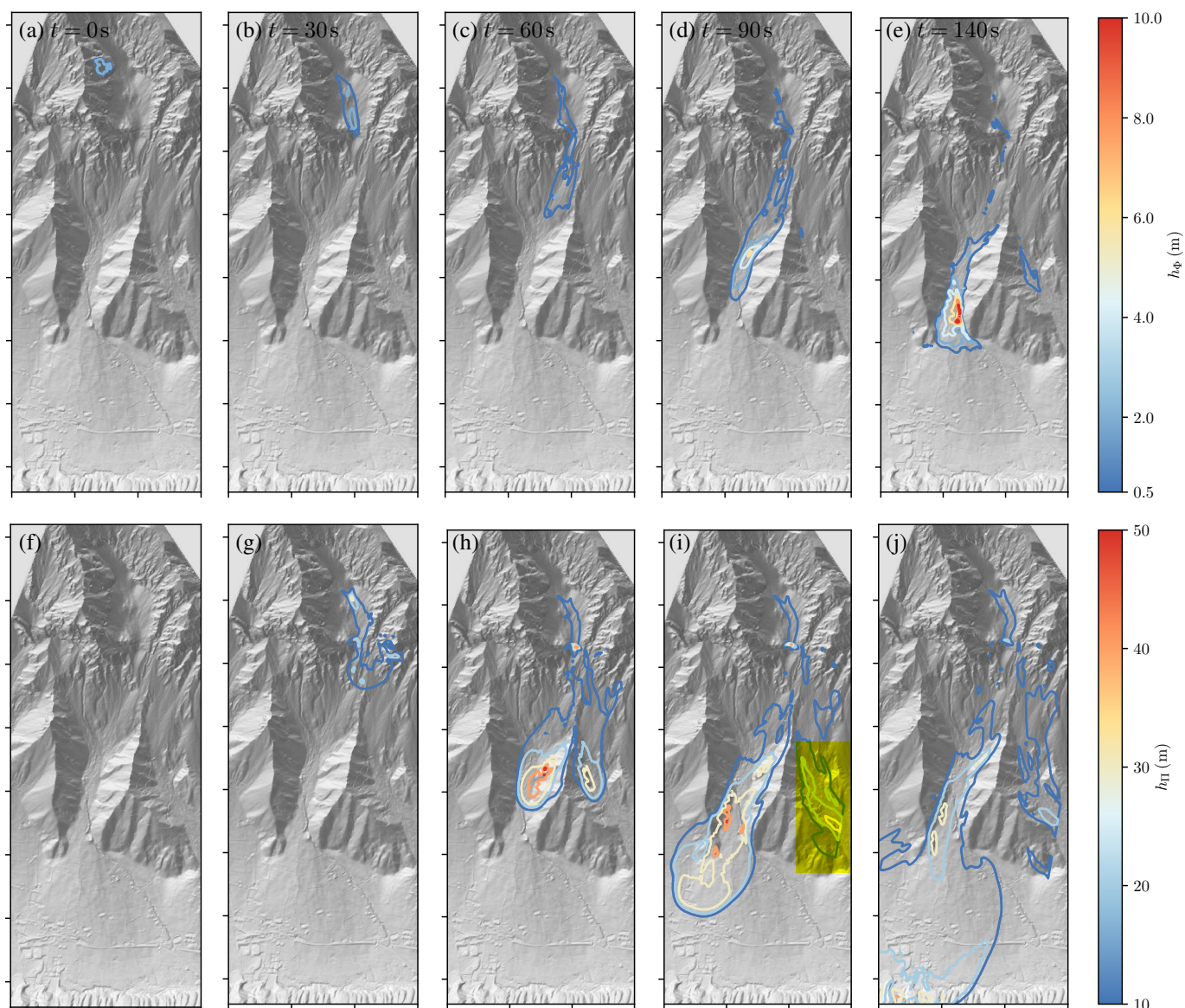


**Figure 12.** Numerical simulation of the Eiskar avalanche with the two layer model. The first row (a-e) shows the height of the dense flow layer, the second row (f-j) shows the height of the powder cloud layer. Each tick on the x- and y-axis corresponds to 500 m.

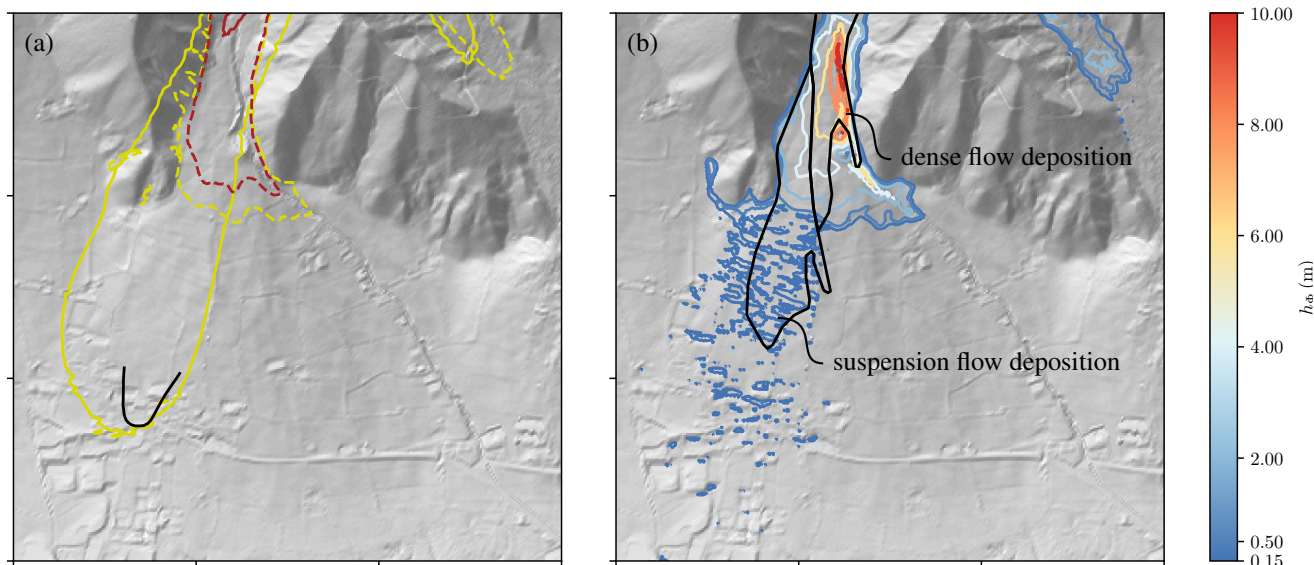


**Figure 13.** (a) The dynamic peak pressure of the suspension layer (solid lines) and the dense flow layer (dashed line). The yellow line marks the 1 kPa isoline and the red line the 10 kPa isoline. The black line marks the limit of the estimated 1 kPa isoline following observations. (b) The deposition of the avalanche (at  $t = 200$  s). The black polygons mark regions of dense flow deposition (above) and powder cloud deposition (below).

Five timesteps of the simulation are shown in Fig. 12 in terms of the dense flow height  $h_{\Phi}$  (a-e) and the suspension flow  
645 height  $h_{\Pi}$  (f-j). The collapsing slab (Fig. 12a) falls down the steep cliff onto a larger snow field where it can entrain additional  
snow. After around 30 s the avalanche reaches a second cliff and a powder cloud starts to emerge (Fig. 12b,g). The suspension  
layer keeps growing substantially in the slope section with an inclination of  $25^{\circ}$  (Fig. 12c, h) and starts to detach when reaching  
the flatter slope of  $10^{\circ}$  inclination. The suspension layer reaches the village of Ramsau after approximately 90 s (Fig. 12i, j)  
while the dense flow comes to a halt at the exit of the valley (Fig. 12d, e). Interestingly the dense flow is pushed towards the  
650 left by terrain features at the exit of the valley while the suspension layer is widely unaffected by these small obstacles.

The corresponding zones of dynamic pressure are shown in Fig. 13a. The 1 kPa isoline of the suspension layer extends wide  
into the village. This fit was used as benchmark to determine the optimal model parameters and thus matches observations  
well. The final deposition of the model is shown in Fig. 13b and compared to the observed deposition. The observed deposition  
could be distinguish between suspension and dense flow depositions (Oesterle, 2019) and the same can be done in the numerical  
655 model. The dense flow layer leaves behind up to 10 m thick deposits (to be corrected by a factor of  $1/3$  to match the deposition  
density) with sharp edges, while the suspension generates deposits with  $0.1 - 0.2$  m thickness (to be corrected as well) that fade  
out gradually. Both, the position of the respective deposits as well as the rough shape match the observations.

Overall the model is able to reproduce the observed flow traces, from the dynamic pressure to the varying snow deposits  
in a single simulation. However, the model parameter had to be fitted to achieve these results. The friction parameters have  
660 to be substantially lower than in the Wolfsgrube case and the coupling factor has to be an order of magnitude higher. This





indicated that either snow conditions were substantially different or that the model does not cover some substantially important processes.

## 8 Conclusions

This work provides an overview over the implementation of the granular dense flow model of Savage and Hutter (1989, 1991) and the suspension flow model of Parker et al. (1986) into OpenFOAM. Further, the models have been combined by means of a novel coupling mechanism to provide a simple yet effective mixed snow avalanche model. These three models form the core of the OpenFOAM avalanche module. The module is accompanied by a new toolchain that substantially simplifies the practical application of the framework. The integration of geographic information system (GIS) file types into the OpenFOAM framework enables a simple and deep integration in existing workflows. Moreover, the dependencies on third party libraries for GIS support were removed as they showed to be missing often on computational clusters. In comparison to the work of Rauter et al. (2018), the models and all tools are integrated into OpenFOAM to simplify installation. The physical models are highly modular. Tweaking and replacing specific empirical relation or process models is a core feature of the framework and highly encouraged.

The implementation of the suspension flow model of Parker et al. (1986) was verified by repeating published results, assuring the absence of implementation errors. A novel two layer model was developed and evaluated with simple synthetic cases. The results are reasonable and follow the expectations set in the model. Further investigations have been conducted with two different real case avalanches. The reach of the dense flow layer and the suspension layer matched the observed runout in both cases with good accuracy, although a quantitative comparison was not conducted. The dense flow of the Wolfsgruben avalanche came short for approximately 20 m, the impact pressure of the suspension flow is reasonable considering the observed damage. Results for the Eiskar avalanche are similarly matching observations well if the parameters are fitted accordingly.

The good results are strongly linked to the parametrisation, which is highly uncertain due to the limited experience with mixed snow avalanche models in general and this model in particular. A wide variety of results can be achieved by tweaking the parameters of the model and substantial investigations will be required to find the appropriate parameters for the large number of semi-empirical relations embedded in the flow models. Substantially different parameters were required to yield reasonable results in both cases, a well known problem in gravitational mass flow modelling (Scheidegger, 1973; Lucas et al., 2014). Further, snow properties and temperatures might have been substantially different between the two avalanche events. In this regard we see a strong opportunity to substantially improve the two layer model. Temperature has a strong influence on the particle diameter distribution in snow avalanches and will thus have a high effect on the mobility and the ability to generate suspension flows (Steinkogler et al., 2015a, b).

The dense flow runout and especially its dynamic pressure at a specific point are very sensitive to the parameters. This is related to the strong friction that rises rapidly in flat regions, where also the driving gravitational acceleration vanishes. The suspension cloud is less sensitive to such influences as the friction is lower and independent of the inclination and the basal pressure. Therefore the suspension runout is less sensitive to the parameters.



For practical applications we **advice** to use the existing guidelines for the dense flow parameters (e.g. Salm et al., 1990).  
695 For snow avalanches with a high potential to generate powder snow clouds, we suggest to apply the suspension and coupling  
parameters as used in the Eiskar case. It should be noted that the suspension model absorbs mass from the dense flow model,  
which reduces the respective runout. Therefore it might be reasonable to simulate scenarios with less powder flow generation to  
not underestimate the runout of the dense core. Finally, it should be kept in mind that the results of the model are accompanied  
by a high amount of uncertainties and that they should be used accordingly. Nevertheless, the simulations presented here  
700 recreate the processes of the events well and provide a considerable amount of additional information.

Generally, the model and the whole framework is aiming to be very flexible to provide researchers with a strong platform to  
develop and evaluate novel friction, entrainment and coupling models. The introduced coupling model represents a reasonable  
approach that yields promising results but there might be large opportunities for improvement. We hope that the framework  
can provide a starting point for other researchers to develop new coupling mechanisms with better performance. Further, new  
705 solvers can be implemented on basis of the framework, e.g. multiphase models for debris flows (e.g. Pudasaini, 2012; Kowalski  
and McElwaine, 2013; Iverson and George, 2014) as done by Garcés et al. (2023) with `faDebrisFoam` or landslide tsunamis  
(e.g. George et al., 2017). The **here presented toolchain and post-processing routines** can be reused with these models and  
additional pre- and postprocessing utilities can be added to enlarge the functionality of the whole framework.

*Code and data availability.* The code is available in the OpenFOAM avalanche repository at <https://develop.openfoam.com/Community/avalanche>  
710 avalanche under the tag v2312. It is further included in the OpenFOAM-v2312 builds and releases (<https://www.openfoam.com/news/main-news/openfoam-v2312>). The 1988 Wolfsgruben avalanche simulation and previous test and validation cases are included as a tutorial in the repository. The code is licensed under GNU General Public License v3, test data is licensed under CC BY 3.0 by Amt der Tiroler Landesregierung (AdTLR).

## Appendix A: Simplified computation of centrifugal forces

715 The basal pressure is computed following Eq. (19) in the **(Savage and Hutter, 1989, 1991) model** (Rauter and Tuković, 2018).  
For the Parker et al. (1986) model we tried to achieve a simpler model that can also be combined with the empirical process  
models in the powder cloud but still follows the general approach. Neglecting the small longitudinal pressure gradient term  
and removing the indices marking the layer, Eq. (19) can be simplified to

$$h\rho\mathbf{g}_n - \xi\rho\nabla_n^\Gamma \cdot (h\bar{\mathbf{u}}\bar{\mathbf{u}}) = -\mathbf{n}^\Gamma p_\Phi. \quad (\text{A1})$$

720 We want to compare this equation to the following equation with an effective gravitational acceleration that contains the effects  
of centrifugal forces,

$$h\rho\mathbf{g}_{\text{eff}} = -\mathbf{n}^\Gamma p_\Phi. \quad (\text{A2})$$



Setting  $\mathbf{n}^\Gamma p_\Phi$  in Eqs. (A1) and (A2) equal to one another yields

$$h\rho\mathbf{g}_{\text{eff}} = h\rho\mathbf{g}_n - \xi\rho\nabla_n^\Gamma \cdot (h\bar{\mathbf{u}}\bar{\mathbf{u}}). \quad (\text{A3})$$

725 After approximating  $\nabla_n^\Gamma \cdot (h\bar{\mathbf{u}}\bar{\mathbf{u}})$  as  $h\nabla_n^\Gamma \cdot (\bar{\mathbf{u}}\bar{\mathbf{u}})$  and dividing by  $h\rho$ , we can write

$$\mathbf{g}_{\text{eff}} \approx \mathbf{g}_n - \xi\nabla_n^\Gamma \cdot (\bar{\mathbf{u}}\bar{\mathbf{u}}). \quad (\text{A4})$$

A further approximation neglects the shape factor  $\xi$ , finally leading to the effective gravitational acceleration as described by Eq. (31).

*Author contributions.* M.R.: Conceptualization, Methodology, Software, Writing. J.K.: Conceptualization, Validation, Writing.

730 *Competing interests.* No competing interests are present.

*Acknowledgements.* We thank Matthias Granig and Felix Oesterle (WLV) for providing, documentation, support and data for the real case examples.



## References

- Ancey, C.: Powder snow avalanches: Approximation as non-Boussinesq clouds with a Richardson number–dependent entrainment function, *Journal of Geophysical Research: Earth Surface*, 109, <https://doi.org/10.1029/2003JF000052>, 2004.
- 735 Bagnold, R. A.: Experiments on a gravity-free dispersion of large solid spheres in a Newtonian fluid under shear, *in: Proceedings of the Royal Society of London A: Mathematical, Physical and Engineering Sciences*, vol. 225, pp. 49–63, The Royal Society, <https://doi.org/10.1098/rspa.1954.0186>, 1954.
- Barker, T. and Gray, J. M. N. T.: Partial regularisation of the incompressible  $\mu(I)$ -rheology for granular flow, *Journal of Fluid Mechanics*, 740 828, 5–32, <https://doi.org/10.1017/jfm.2017.428>, 2017.
- Barker, T., Rauter, M., Maguire, E., Johnson, C., and Gray, J.: Coupling rheology and segregation in granular flows, *Journal of Fluid Mechanics*, 909, A22, <https://doi.org/10.1017/jfm.2020.973>, 2021.
- Barré de Saint-Venant, A. J. C.: Théorie du mouvement non permanent des eaux, avec application aux crues des rivières et à l'introduction des marées dans leurs lits, *Comptes Rendus des séances de l'Académie des Sciences*, 73, 237–240, 1871.
- 745 Bartelt, P., Buser, O., Vera Valero, C., and Bühler, Y.: Configurational energy and the formation of mixed flowing/powder snow and ice avalanches, *Annals of Glaciology*, 57, 179–188, <https://doi.org/10.3189/2016AoG71A464>, 2016.
- Bouchut, F. and Westdickenberg, M.: Gravity driven shallow water models for arbitrary topography, *Communications in Mathematical Sciences*, 2, 359–389, 2004.
- Bouchut, F., Mangeney-Castelnaud, A., Perthame, B., and Vilotte, J.-P.: A new model of Saint Venant and Savage–Hutter type for gravity driven shallow water flows, *Comptes Rendus Mathématique*, 336, 531 – 536, [https://doi.org/10.1016/S1631-073X\(03\)00117-1](https://doi.org/10.1016/S1631-073X(03)00117-1), 2003.
- 750 Boyer, F., Guazzelli, É., and Pouliquen, O.: Unifying suspension and granular rheology, *Physical Review Letters*, 107, 188 301, <https://doi.org/10.1103/PhysRevLett.107.188301>, 2011.
- Christen, M., Kowalski, J., and Bartelt, P.: RAMMS: Numerical simulation of dense snow avalanches in three-dimensional terrain, *Cold Regions Science and Technology*, 63, 1–14, <https://doi.org/10.1016/j.coldregions.2010.04.005>, 2010.
- 755 Craster, R. V. and Matar, O. K.: Dynamics and stability of thin liquid films, *Reviews of Modern Physics*, 81, 1131–1198, <https://doi.org/10.1103/RevModPhys.81.1131>, 2009.
- Deckelnick, K., Dziuk, G., and Elliott, C. M.: Computation of geometric partial differential equations and mean curvature flow, *Acta numerica*, 14, 139–232, <https://doi.org/10.1017/S0962492904000224>, 2005.
- Denlinger, R. P. and Iverson, R. M.: Granular avalanches across irregular three-dimensional terrain: 1. Theory and computation, *Journal of Geophysical Research: Earth Surface*, 109, F01 014, <https://doi.org/10.1029/2003JF000085>, 2004.
- 760 Dieter-Kissling, K., Marschall, H., and Bothe, D.: Numerical method for coupled interfacial surfactant transport on dynamic surface meshes of general topology, *Computers & Fluids*, 109, 168–184, <https://doi.org/10.1016/j.compfluid.2014.12.017>, 2015.
- Ferziger, J. H. and Peric, M.: *Computational methods for fluid dynamics*, Springer, 3 edn., 2002.
- Fischer, J.-T., Kowalski, J., and Pudasaini, S. P.: Topographic curvature effects in applied avalanche modeling, *Cold Regions Science and Technology*, 74, 21–30, <https://doi.org/10.1016/j.coldregions.2012.01.005>, 2012.
- 765 Fischer, J.-T., Kofler, A., Wolfgang, F., Granig, M., and Kleemayr, K.: Multivariate parameter optimization for computational snow avalanche simulation in 3d terrain, *Journal of Glaciology*, 61, 875–888, <https://doi.org/10.3189/2015JoG14J168>, 2015.
- Forterre, Y. and Pouliquen, O.: Flows of Dense Granular Media, *Annu. Rev. Fluid Mech.*, 40, 1–24, <https://doi.org/10.1146/annurev.fluid.40.111406.102142>, 2008.



- 770 Garcés, A., González, Á., Tamburrino, A., and Montserrat, S.: faDebrisFOAM validation using field data surveyed in Crucecita (Chile) alluvial fan for the event of 13th May 2017, in: E3S Web of Conferences, vol. 415, p. 02007, EDP Sciences, <https://doi.org/10.1051/e3sconf/202341502007>, 2023.
- George, D. L., Iverson, R. M., and Cannon, C. M.: New methodology for computing tsunami generation by subaerial landslides: Application to the 2015 Tyndall Glacier landslide, Alaska, *Geophysical Research Letters*, 44, 7276–7284, <https://doi.org/10.1002/2017GL074341>, 775 2017.
- Hagemeier, T., Hartmann, M., and Thévenin, D.: Practice of vehicle soiling investigations: A review, *International Journal of Multiphase Flow*, 37, 860–875, <https://doi.org/10.1016/j.ijmultiphaseflow.2011.05.002>, 2011.
- Heerema, C. J., Talling, P. J., Cartigny, M. J., Paull, C. K., Bailey, L., Simmons, S. M., Parsons, D. R., Clare, M. A., Gwiazda, R., Lundsten, E., et al.: What determines the downstream evolution of turbidity currents?, *Earth and Planetary Science Letters*, 532, 116023, 2020.
- 780 Hergarten, S. and Robl, J.: Modelling rapid mass movements using the shallow water equations in Cartesian coordinates, *Natural Hazards and Earth System Sciences*, 15, 671–685, <https://doi.org/10.5194/nhess-15-671-2015>, 2015.
- Huber, A., Kofler, A., Rauter, M., Fischer, J.-T., and Adams, M. S.: Simulation of dense snow avalanches with open source software, in: *Proceedings of the International Snow Science Workshop, Innsbruck, Austria*, 2018.
- Issler, D., Jenkins, J. T., and McElwaine, J. N.: Comments on avalanche flow models based on the concept of random kinetic energy, *Journal of Glaciology*, 64, 148–164, <https://doi.org/10.1017/jog.2017.62>, 2018.
- 785 Iverson, R. M. and George, D. L.: A depth-averaged debris-flow model that includes the effects of evolving dilatancy. I. Physical basis, *Proceedings of the Royal Society of London A: Mathematical, Physical and Engineering Sciences*, 470, <https://doi.org/10.1098/rspa.2013.0819>, 2014.
- Jasak, H.: Error analysis and estimation for the finite volume method with applications to fluid flows, Ph.D. thesis, Imperial College, University of London, 1996.
- 790 Jóhannesson, T., Gauer, P., Issler, P., and Lied, K.: The design of avalanche protection dams. Recent practical and theoretical developments, No. EUR 23339 in *Climate Change and Natural Hazard Research Series 2*, 978-92-79-08885-8, 2009.
- Juretić, F.: cfMesh User Guide, *Creative Fields, Zagreb*, 2015.
- Köhler, A., McElwaine, J., and Sovilla, B.: GEODAR data and the flow regimes of snow avalanches, *Journal of geophysical research: earth surface*, 123, 1272–1294, <https://doi.org/10.1002/2017JF004375>, 2018.
- 795 Kowalski, J. and McElwaine, J. N.: Shallow two-component gravity-driven flows with vertical variation, *Journal of Fluid Mechanics*, 714, 434–462, <https://doi.org/10.1017/jfm.2012.489>, 2013.
- Kowalski, J. and Torrilhon, M.: Moment *Approximations and Model Cascades for Shallow Flow*, *Communications in Computational Physics*, 25, 669–702, <https://doi.org/10.4208/cicp.OA-2017-0263>, 2019.
- 800 LeVeque, R. J.: *Finite volume methods for hyperbolic problems, vol. 31*, Cambridge University Press, 2002.
- Løvholt, F., Pedersen, G., Harbitz, C. B., Glimsdal, S., and Kim, J.: On the characteristics of landslide tsunamis, *Philosophical Transactions of the Royal Society A*, 373, 20140376, <https://doi.org/10.1098/rsta.2014.0376>, 2015.
- Lucas, A., Mangeney, A., and Ampuero, J. P.: Frictional velocity-weakening in landslides on Earth and on other planetary bodies, *Nature Communications*, 5, 1–9, <https://doi.org/10.1038/ncomms4417>, 2014.
- 805 Meiburg, E., Radhakrishnan, S., and Nasr-Azadani, M.: Modeling gravity and turbidity currents: computational approaches and challenges, *Applied Mechanics Reviews*, 67, 040802, <https://doi.org/10.1115/1.4031040>, 2015.



- Mergili, M., Fischer, J.-T., Krenn, J., and Pudasaini, S. P.: r.avaflow v1, an advanced open-source computational framework for the propagation and interaction of two-phase mass flows, *Geoscientific Model Development*, 10, 553–569, <https://doi.org/10.5194/gmd-10-553-2017>, 2017.
- 810 Moukalled, F., Mangani, L., Darwish, M., et al.: *The finite volume method in computational fluid dynamics*, Springer, <https://doi.org/10.1007/978-3-319-16874-6>, 2016.
- Oesterle, F.: *Eiskar-Avalanche event January 2019 (german)*, *Technischer Bericht/Nachrechnung, Wildbach- und Lawinenverbauung - Fachzentrum Geologie und Lawinen*, 2019.
- Parker, G., Fukushima, Y., and Pantin, H. M.: Self-accelerating turbidity currents, *Journal of Fluid Mechanics*, 171, 145–181, <https://doi.org/10.1017/S0022112086001404>, 1986.
- 815 Pitman, E. B., Nichita, C. C., Patra, A., Bauer, A., Sheridan, M., and Bursik, M.: Computing granular avalanches and landslides, *Physics of Fluids*, 15, 3638–3646, <https://doi.org/10.1063/1.1614253>, 2003.
- Pudasaini, S. P.: A general two-phase debris flow model, *Journal of Geophysical Research: Earth Surface*, 117, <https://doi.org/10.1029/2011JF002186>, 2012.
- 820 Pudasaini, S. P. and Hutter, K.: *Avalanche Dynamics: Dynamics of Rapid Flows of Dense Granular Avalanches*, Springer, <https://doi.org/10.1007/978-3-540-32687-8>, 2007.
- Pudasaini, S. P., Wang, Y., and Hutter, K.: Rapid motions of free-surface avalanches down curved and twisted channels and their numerical simulation, *Philosophical Transactions of the Royal Society of London A: Mathematical, Physical and Engineering Sciences*, 363, 1551–1571, <https://doi.org/10.1098/rsta.2005.1595>, 2005.
- 825 Rastello, M., Rastello, F., Bellot, H., Ousset, F., Dufour, F., and Meier, L.: Size of snow particles in a powder-snow avalanche, *Journal of Glaciology*, 57, 151–156, 2011.
- Rauter, M.: The compressible granular collapse in a fluid as a continuum: validity of a Navier-Stokes model with  $\mu(J), \phi(J)$ -rheology, *Journal of Fluid Mechanics*, 915, <https://doi.org/10.1017/jfm.2021.107>, 2021.
- Rauter, M. and Köhler, A.: Constraints on entrainment and deposition models in avalanche simulations from high-resolution radar data, *Geosciences*, 10, 9, <https://doi.org/10.3390/geosciences10010009>, 2020.
- 830 Rauter, M. and Tuković, Ž.: A finite area scheme for shallow granular flows on three-dimensional surfaces, *Computer & Fluids*, <https://doi.org/10.1016/j.compfluid.2018.02.017>, 2018.
- Rauter, M., Fischer, J.-T., Fellin, W., and Kofler, A.: Snow avalanche friction relation based on extended kinetic theory, *Natural Hazards and Earth System Sciences*, 16, 2325–2345, <https://doi.org/10.5194/nhess-16-2325-2016>, 2016.
- 835 Rauter, M., Kofler, A., Huber, A., and Fellin, W.: faSavageHutterFOAM 1.0: depth-integrated simulation of dense snow avalanches on natural terrain with OpenFOAM, *Geoscientific Model Development*, 11, 2923–2939, <https://doi.org/10.5194/gmd-11-2923-2018>, 2018.
- Rauter, M., Viroulet, S., Gylfadóttir, S. S., Fellin, W., and Løvholm, F.: Granular porous landslide tsunami modelling—the 2014 Lake Askja flank collapse, *Nature communications*, 13, 678, <https://doi.org/10.1038/s41467-022-28296-7>, 2022.
- Roache, P. J.: Quantification of uncertainty in computational fluid dynamics, *Annual Review of Fluid Mechanics*, 29, 123–160, <https://doi.org/10.1146/annurev.fluid.29.1.123>, 1997.
- 840 Salm, B., Gubler, H. U., and Burkard, A.: *Berechnung von Fliesslawinen: eine Anleitung für Praktiker mit Beispielen*, *Tech. rep.*, WSL Institut für Schnee-und Lawinenforschung SLF, Davos, 1990.
- Sampl, P. and Zwinger, T.: Avalanche simulation with SAMOS, *Annals of Glaciology*, 38, 393–398, <https://doi.org/10.3189/172756404781814780>, 2004.



- 845 Savage, S. B. and Hutter, K.: The motion of a finite mass of granular material down a rough incline, *Journal of Fluid Mechanics*, 199, 177–215, <https://doi.org/10.1017/S0022112089000340>, 1989.
- Savage, S. B. and Hutter, K.: The dynamics of avalanches of granular materials from initiation to runout. Part I: Analysis, *Acta Mechanica*, 86, 201–223, <https://doi.org/10.1007/BF01175958>, 1991.
- Scheidegger, A. E.: On the prediction of the reach and velocity of catastrophic landslides, *Rock Mechanics and Rock Engineering*, 5, 231–
- 850 236, <https://doi.org/10.1007/BF01301796>, 1973.
- Shimizu, H. A.: Numerical **Simulations of Dome-Collapse Pyroclastic Density Currents Using** faSavageHutterFOAM: Application to the 3 June 1991 Eruption of Unzen Volcano, Japan, *Journal of Disaster Research*, 17, 768–778, <https://doi.org/10.20965/jdr.2022.p0768>, 2022.
- Sovilla, B., McElwaine, J. N., and Louge, M. Y.: The structure of powder snow avalanches, *Comptes Rendus Physique*, 16, 97–104, <https://doi.org/10.1016/j.crhy.2014.11.005>, 2015.
- 855 Steinkogler, W., Gaume, J., Löwe, H., Sovilla, B., and Lehning, M.: Granulation of snow: From tumbler experiments to discrete element simulations, 120, 1107–1126, <https://doi.org/10.1002/2014JF003294>, 2015a.
- Steinkogler, W., Sovilla, B., and Lehning, M.: Thermal energy in dry snow avalanches, *Cryosphere*, 9, 1819–1830, <https://doi.org/10.5194/tc-9-1819-2015>, 2015b.
- Tuković, Ž. and Jasak, H.: A moving mesh finite volume interface tracking method for surface tension dominated interfacial fluid flow,
- 860 *Computers & Fluids*, 55, 70–84, <https://doi.org/doi:10.1016/j.compfluid.2011.11.003>, 2012.
- Turnbull, B. and Bartelt, P.: Mass and momentum balance model of a mixed flowing/powder snow avalanche, *Surveys in Geophysics*, 24, 465–477, <https://doi.org/10.1023/B:GEOP.0000006077.82404.84>, 2003.
- Turner, J.: Turbulent entrainment: the development of the entrainment assumption, and its application to geophysical flows, *Journal of Fluid Mechanics*, 173, 431–471, <https://doi.org/10.1017/S0022112086001222>, 1986.
- 865 Vescovi, D., di Prisco, C., and Berzi, D.: From solid to granular gases: the steady state for granular materials, *International Journal for Numerical and Analytical Methods in Geomechanics*, 37, 2937–2951, <https://doi.org/10.1002/nag.2169>, 2013.
- Viroulet, S., Baker, J., Edwards, A., Johnson, C. G., Gjaltema, C., Clavel, P., and Gray, J.: Multiple solutions for granular flow over a smooth two-dimensional bump, *Journal of Fluid Mechanics*, 815, 77–116, <https://doi.org/10.1017/jfm.2017.41>, 2017.
- Voellmy, A.: Über die Zerstörungskraft von Lawinen (On the destructive forces of avalanches), *Schweizerische Bauzeitung*, 73 (15), 212–
- 870 217, <https://doi.org/10.5169/seals-61891>, 1955.
- Zhao, H. and Kowalski, J.: Bayesian active learning for parameter calibration of landslide run-out models, *Landslides*, 19, 2033–2045, <https://doi.org/10.1007/s10346-022-01857-z>, 2022.